Quantitative Determination of Pyrite by Mossbauer Spectroscopy

by

Thomas W. Guettinger

ProQuest LLC.
789 East Eisenhower Parkway
P.O. Box 1346
Ann Arbor, MI 48106 – 1346

T-2264

A thesis submitted to the Faculty and the Board of Trustees of the Colorado School of Mines in partial fulfillment of the requirements for the degree of Master of Science, Physics.

Golden, Colorado

Date 26 Nov., 1979

Signed: _____
Thomas W. Guettinger

Golden, Colorado

Date 14 Dec., 1979

Approved: _____
Dr. D.L. Williamson
Thesis Advisor

Golden, Colorado

Date 12-14, 1979

_____
Dr. F.D. Schowengerdt
Head of Department of Physics

ABSTRACT

The relative resonance intensity of the two Mossbauer transitions at ^{57}Fe sites in pyrite (FeS_2) is found experimentally to be unity (0.997 ± 0.004) and independent of the single crystal orientation relative to the γ-ray direction. This result is consistent with a recent prediction of an angle independent quadrupole interaction peculiar to the symmetry of pyrite and also demonstrates the recoil-free fraction f to be isotropic within experimental error. These results permit one to disregard pyrite crystal orientation in a textured coal sample and the amount of pyrite can be determined solely from one of the two transition lines.

Pyrite crystals occur in coals in various sizes and shapes. The effect of granularity of the Mossbauer absorber on the spectral lines of pyrite is shown to result in a substantial increase in the resonance area for smaller particles in powder absorbers of constant pyrite mass per unit area. The calculations of previous works are carried out to second order correction terms and a Gaussian particle size distribution is considered.

It is found that inclusion of the second order correction offers no substantial improvement over a simple first order correction, particularly for larger particle sizes. The Gaussian distribution is found to alter the first order correction term in such a way as to cause a larger decrease

in resonance area compared to particles of uniform size. Extrapolation of the experimental pyrite resonance area to zero average partial size leads to $f = 0.80 \pm .08$.

TABLE OF CONTENTS

LIST OF ILLUSTRATIONS

LIST OF TABLES

ACKNOWLEDGEMENTS

I am deeply grateful to my thesis advisor, Dr. D.L. Williamson, for his continuous support, advice and endless patience without which I could not have written this thesis.

I thank the members of my thesis committee, Dr. E. Cecil for providing me with some of the basic knowledge and Dr. D. Dickerhoof for his assistance and for providing the crystal pyrite.

The assistance of various ladies and gentlemen, who have given me advice on several subjects of this thesis, expecially Dr. Rex Bull, Dr. G. Krauss and Dr. C. Baer, is sincerely appreciated.

My gratitude goes to the Graduate School of the Colorado School of Mines and the Mining and Mineral Resources Center (MRC) for supporting this work with a Research Assistantship and a MRC Fellowship, respectively.

Special thanks are given to my mother, Mrs. P. Guettinger and father Dr. W. Guettinger, who convinced me quite early of the necessity of understanding physics as a basis of all science.

I am also much indebted to my friends, Christian R. and Pamela C. Bergman, for their invaluable support.

INTRODUCTION

In the last decade Mossbauer effect spectroscopy (MES) has become a powerful tool in qualitative analysis of various minerals, particularily those containing iron (Fe). One of the new regions of interest is the analysis of coal and coal related substances. Several papers list MES data on Fe-minerals and transformation products found in coals [1-10], coke[8], shale [6,11], hydrogenation products [9] and volatile matter residue [8]. This thesis is concerned with iron sulfide (pyrite, FeS_2), which occurs in many of the above substances. The amount of pyrite is most commonly determined by standard chemical analysis (ASTM). Reference (3) discusses the problems involved in the use of this chemical method, resulting in inaccuracies of up to 20%.

MES is a method for identification of pyrite and may become an alternative technique for its quantitative determination in coals and their transformed phases after processes such as coking and liquefaction. One of the advantages of MES for this purpose is the relatively short time needed, less than a couple of hours once the method is properly developed, while ASTM-analysis requires a day.

So far however, two effects have been given little or no concern in the quantitative determination of pyrite in coal by MES: the angle dependence of the Mossbauer effect and the

effect of inhomogeneity of the absorber under examination. The angle dependence deserves examination since one of the two transition lines of pyrite in coal usually overlaps with a Fe^{2+} line resulting in a difference in line intensity and width. If the two pyrite lines have equal intensities, independent of the orientation of the pyrite to the γ-ray beam, the undisturbed line alone can be used in quantitative analysis. Since pyrite occurs in coal in granular form of various shape and size the effect of this inhomogeneity on MES needs to be studied.

This work will try to clarify these problems and include a careful analysis of an additional experimental problem due to background radiation. Section 1 offers a brief description of the Mossbauer parameters involved. The angle dependence of MES in pyrite is examined in section 2 and section 3 treats the effects of absorber inhomogeneity and background radiation.

1. THE MOSSBAUER EFFECT

1.1 Theory

Mossbauer or gamma-resonance spectroscopy is based on processes in γ-ray emission and absorption that possess a certain probability of being recoil-free.

Consider a free nucleus of mass M emitting a γ-ray of energy E_γ by a nuclear transition from an excited to the ground state. The nucleus will experience a recoil of energy E_R and conservation of energy requires

$$E_\gamma + E_R = E_o \tag{1.1}$$

where E_o is the nuclear transition energy. The nucleus, originally at rest, will gain a momentum P_n according to

$$E_R = \frac{P_n^2}{2M} \quad . \tag{1.2}$$

The momentum of the γ-ray is given by

$$P_\gamma = \frac{E_\gamma}{C} = \hbar k \tag{1.3}$$

where C is the velocity of light, k is the magnitude of the wave vector of the γ-ray and $\hbar$ is Planck's constant divided by 2π . Conservation of momentum yields

$$E_R = \frac{P_\gamma^2}{2M} = \frac{E_\gamma^2}{2MC^2} \tag{1.4}$$

(Since $E_R << MC^2$ the problem can be treated nonrelativistically).

For absorption processes the above calculations also hold except for a sign change of E_R in eqn. (1.1). The resulting emission and absorption lines are shifted as in Fig. 1.1. Thermal Doppler broadening may result in a small overlap of emission and absorption lines to make nuclear resonance fluorescence possible.

Now consider the γ-ray emission of an atom bound in a solid. Three processes may occur:

a) The recoil energy is above the threshold displacement energy; then the atom knocks itself from its lattice site.

b) The recoil energy E_R is insufficient to displace the atom, but sufficient for thermal excitation of the lattice through phonon creation.

c) The recoil energy is small compared to phonon energies; now a quantum mechanical approach becomes necessary. The result is the existence of zero-phonon transitions, emission processes without phonon excitation in the lattice. The probability f of such processes is called the recoil-free fraction or Debye-Waller factor. Assuming harmonic interaction forces in the solid

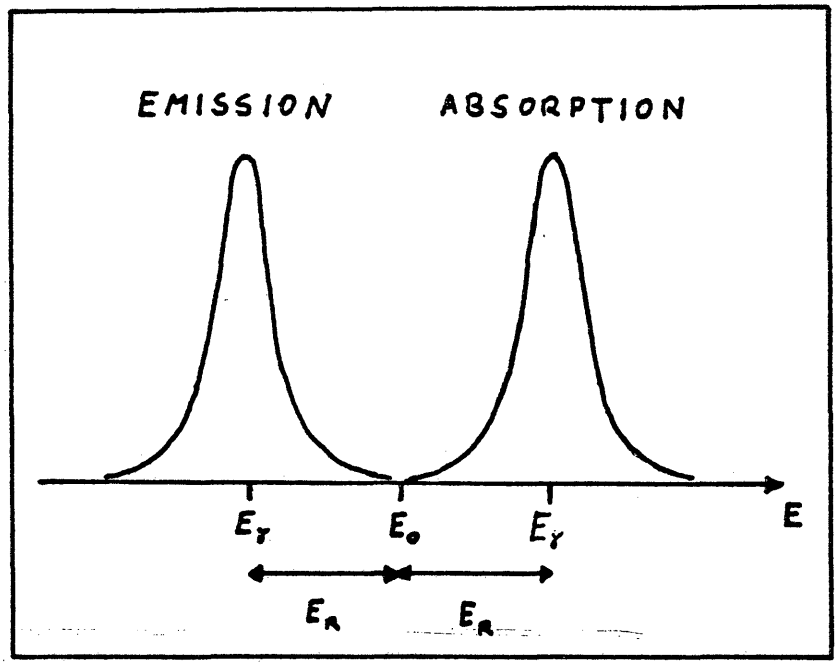

Fig. 1.1. Emission and absorption lines shifted by E_R.

$$f = \exp\left(-k^2 \langle x^2 \rangle\right) \tag{1.5}$$

where $\langle x^2 \rangle$ is the mean square vibrational amplitude in the x-direction. In general, f may be anisotropic if for example $\langle x^2 \rangle \neq \langle y^2 \rangle$.

We now find a discrete narrow line, the Mossbauer line, at E_o in the emission spectrum; $E_o = E_\gamma$ since $E_R \approx 0$ and f is represented quantitatively by the intensity of the Mossbauer line.

What makes the Mossbauer effect so attractive is the extremely narrow line width of the Mossbauer line. From Heisenberg's uncertainty principle

$$\Delta E \cdot \Delta t \geq \hbar \tag{1.6}$$

and one finds $$\Delta E = \Gamma \geq \frac{\hbar}{\tau} = \frac{\ell n 2}{t_{1/2}} \tag{1.7}$$

where Δ indicates the uncertainties in the properties E and t, τ is the mean lifetime of the excited state and $t_{1/2} = \tau \ell n 2$ is its halflife. For example for the 14.4 keV transition in ^{57}Fe $t_{1/2} \approx 10^{-7}$sec, thus $\Gamma \approx 5 \times 10^{-9}$ eV and $\Gamma/E_\gamma \approx 3 \times 10^{-13}$. The Mossbauer effect thus enables us to detect very small changes in relative energies of emitted and absorbed γ-rays.

The number of lines and their positions are influenced by hyperfine interactions, which consist of interactions

between a nuclear (moment) property and an electronic or atomic property. The hyperfine interactions of importance in this work are the isomer shift and the quadrupole splitting.

The isomer shift or "chemical shift" is the result of coulombic interaction of the nuclear charge distribution over a finite nuclear radius in the excited and ground state and the electron charge density at the nucleus (s-electrons). This interaction changes the levels of the ground and excited state and also the transition energies of source and absorber. The difference between the transition energy of the source and the transition energy of the absorber is observed as the isomer shift δ (Fig. 1.2).

The isomer shift is dependent on the relative change of the nuclear radius between excited state and ground state, the difference in total electron density, evaluated at the nucleus, between source and absorber isotopes and nuclear parameters of the given isotopes. The nuclear charge distribution can be assumed to be uniform and spherically symmetric for purposes of a perturbation calculation of δ.

Many nuclei, however, show a deviation from spherical symmetry in their charge distribution, differing in each excitation state. The resulting nuclear electric quadrupole moment eQ, a tensor quantity with elements

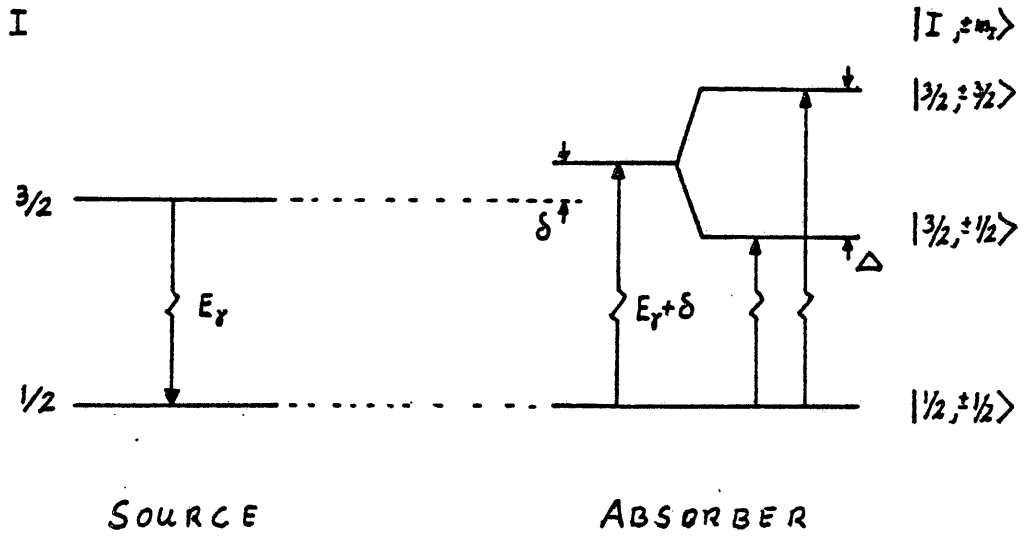

Fig. 1.2. Isomer shift δ and quadrupole splitting Δ for ^{57}Fe.

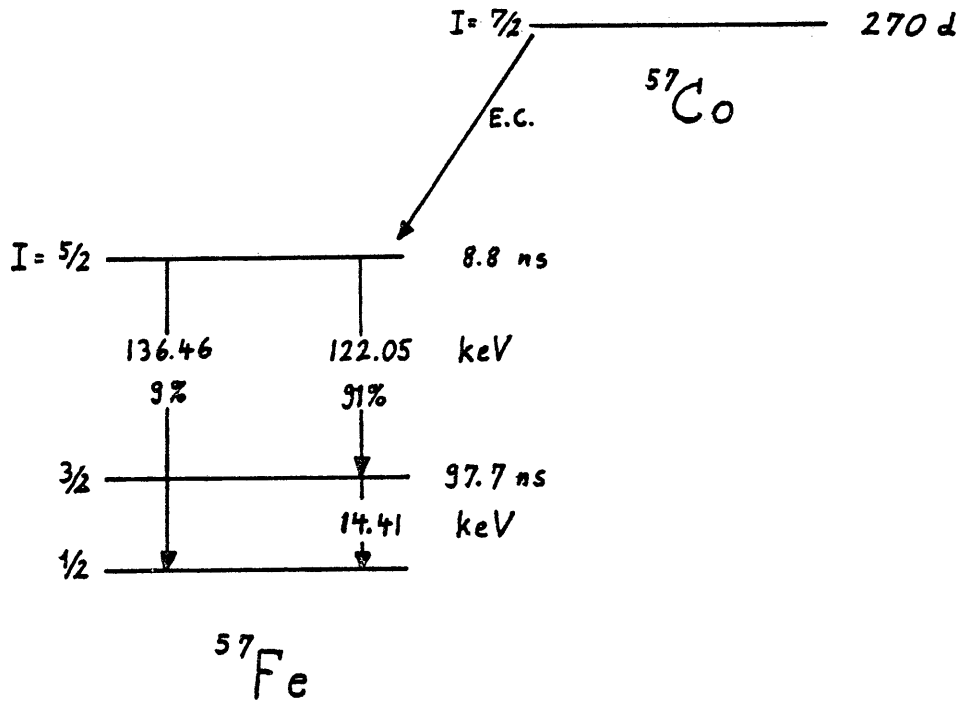

Fig. 1.3. Decay of ^{57}Co to ^{57}Fe.

$$Qij = \int \rho_n(r)\, X_i X_j d^3r \qquad (1.8)$$

(ρ_n = nuclear charge distribution; X_i, X_j are cartesian coordinates of r; e = electron charge), may interact with an inhomogeneous electric field at the nucleus, described by the electric field gradient (EFG), giving rise to quadrupole splitting. The nuclear state is split into sublevels with eigen-values [12]

$$E_Q = \frac{eQV_{zz}}{4I(2I-1)} \left[3m_I^2 - I(I+1) \right] \left(1 + \frac{\eta^2}{3}\right)^{\frac{1}{2}} \qquad (1.9)$$

where $V_{zz} = \frac{\partial^2 V}{\partial z^2}$ is the principal component of the diagonalized EFG-tensor. The EFG is the gradient of the electric field at the nucleus due to a potential V(r) caused by charges at a distance r from the nucleus. With respect to the principal axes the EFG tensor is described by two independent parameters V_{zz} and the asymmetry parameter η defined by

$$\eta = (V_{xx} - V_{yy})/V_{zz} \quad . \qquad (1.10)$$

I is the nuclear spin quantum number and m_I = I, I-1, ..., -I is the nuclear magnetic spin quantum number.

The effect of the electric quadrupole interaction is: a nuclear state with I > 1/2, which is (2I + 1) - fold degenerate, will be split into substates $|I, \pm m_I>$; the double degeneracy can be removed by magnetic perturbation (Nuclear

Zeeman effect) and a description of this interaction can be found in references (12,13,14).

Fig. 1.2 shows the effect of the isomer shift δ and the electric quadrupole interaction Δ for ^{57}Fe, where I = 3/2 for the excited state and I = 1/2 for the ground state.

1.2 Experimental Spectroscopy

The most common isotope used for MES is ^{57}Fe. Fig. 1.3 shows the decay processes in the source. ^{57}Co (halflife 270 days) decays by electron capture (E.C.) to the 136.5 keV state of ^{57}Fe which either decays directly to the ground state by emitting a 136.5 keV gamma or to the 14.4 keV state by emitting a 122 keV gamma. The latter takes place about 91% of the time. The 14.4 keV state now decays to the ground state by γ-ray emission. The γ-ray may transmit its energy to the atomic shell, resulting in the emission of X-rays or electrons (conversion). The γ-decay of the 14.4 keV state is most commonly used for resonance absorption.

As mentioned previously, the resonance lines are extremely sharp and even the best γ-ray detector cannot resolve them. The energy of the γ-ray can be slightly varied by the first-order Doppler effect, i.e. by an appropriate relative motion $\vec{v}$, the nuclear transitions in source and absorber can be matched and resonance occurs. The Doppler effect causes E_γ to be, for emission processes,

$$E_\gamma = E_0 - E_R + E_D \tag{1.11}$$

where $E_D = \frac{v}{c} E_\gamma$ and $E_R \approx 0$. Conventionally the spectrum is not plotted as a function of E_D but rather as a function of the relative velocity v, of the order of mm/sec for ^{57}Fe.

A typical spectrum is shown in Fig. 1.4, using a pyrite (FeS_2) powder absorber and observing the 14.4 keV γ-rays in the transmission mode. The isomer shift and quadrupole splitting ($\delta \simeq 0.31$ mm/sec wrt. Fe-metal and $\Delta \simeq 0.62$ mm/sec for pyrite) caused by the splitting shown in Fig. 1.2 thus provide a means of Fe- compound identification. Paramagnetic susceptibility studies [15] have shown that pyrite is a Fe^{2+} compound with the Fe in a low spin state. This is consistent with the above values of δ and Δ.

The spectra are usually fitted with a superposition of Lorentzian lines and the experimental resonance area of the i-th line is

$$A_i = \frac{\pi}{2} \Gamma_i \frac{N_\infty - N_i}{N_\infty} = \frac{\pi}{2} \frac{\Gamma_i I_i}{N_\infty} \qquad (1.12)$$

Γ_i is the full width at half maximum, N_i is the number of counts at maximum resonance of the i-th line, its intensity is $I_i = N_\infty - N_i$ and N_∞ is the off-resonance count rate, i.e. at $\upsilon = \pm \infty$.

A more detailed description of the theory and methodology in MES can be found in refs. (12-14). References (16,17, 18) present the pyrite lattice structure and associated parameters.

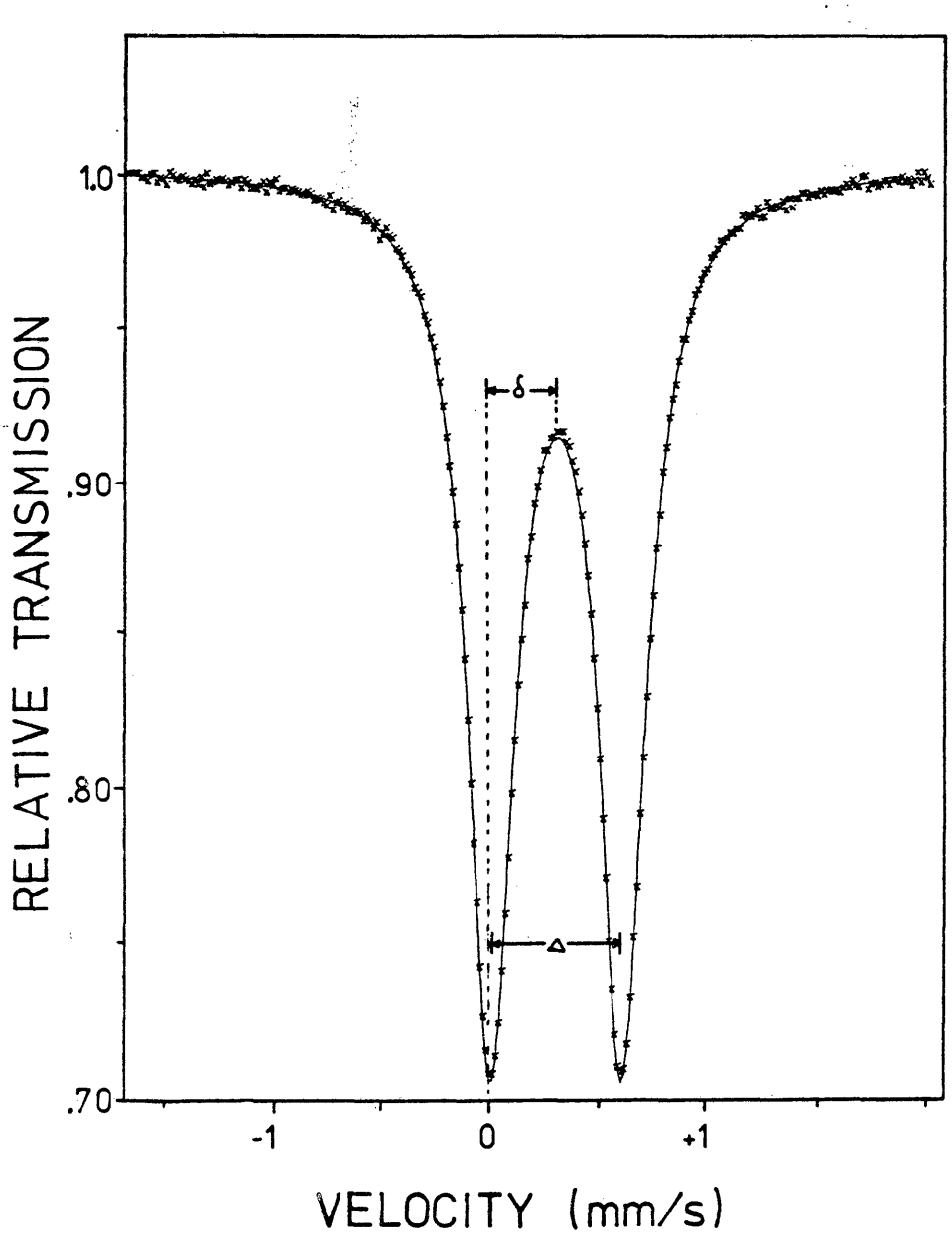

Fig. 1.4. Transmission spectrum for a pure pyrite powder absorber. Indicated are the isomer shift δ and the quadrupole splitting Δ.

2. ANGLE DEPENDENCE OF THE MOSSBAUER EFFECT IN SINGLE CRYSTAL PYRITE*

The presence of an electric field gradient (EFG) at each Fe site in pyrite causes a two line Mossbauer resonance associated with the $\Delta m = \pm \frac{3}{2}$ to $\pm \frac{1}{2}$ and $\Delta m = \pm \frac{1}{2}$ to $\pm \frac{1}{2}$ transitions in ^{57}Fe (Fig. 1.4). In recent papers, Liu[19] evaluates the EFG tensor and mean square displacement (MSD) tensor for each of the four equivalent, but differently oriented, Fe sites in a unit cell. He arrives at a relation between the area ratio of the two Mossbauer resonance lines and the orientation of a single crystal absorber of pyrite with respect to the angles of the incident γ-ray. From this relation a vibrational anisotropy parameter can be determined experimentally as a function of the incident angles. Liu demonstrates from symmetry considerations that the quadrupole interaction is independent of these angles and therefore concludes that, for a single crystal of pyrite, the recoil free fraction is isotropic (vibrational anisotropy parameter = 0) if the area ratio is always unity independent of the crystal orientation.

Prior experimental work (16,17,18) as summarized in Table 5 of reference (16) reveals discrepancies in the obtained area ratios, several of which are different from unity.

*T.W. Guettinger and D.L. Williamson, Phys. Rev. 20B,3938(1979)

All of these experiments were carried out in the transmission mode using relatively thick absorbers of 50μ - 200μ. Because of thickness saturation effects[20], a reduction of area ratio sensitivity of about a factor of three or more can be expected in measurements using such thick absorbers.

2.1 Experimental Technique

To avoid thickness saturation effects and difficulties in preparing thin sections of a pyrite single crystal, we observed the scattered 6.3 keV x-rays produced by the internal conversion process. The preference of the 6.3 keV x-ray to the 14.4 keV γ-rays lies in a higher count rate (internal conversion coefficient = 8.2) and in the smaller effective thickness being sampled, about 20μ, due to electronic absorption of the low energy x-ray.

The crystal used was a naturally occurring specimen which contained the following upper limits, in wt.%, of these elements according to x-ray fluorescene: P - .05, Si - .06, Ca - .03, Ti - .02, V - .02, Ni - .16, Cu - .09, Mo - .15, Ba - .02. The crystal was cut normal to a <100> axis and mounted such that the incident γ-ray could be varied between a <100> and a <110> direction and defined by the angle θ shown in Fig. 2.1. Also shown in the figure is the data for an incident angle $\theta = 60^{o}$.

The data reduction was done by least-squares fitting of Lorentzians to the experimental data. Due to the slight overlap of the two resonance lines (Fig. 2.1) two types of fits were used: one which allowed independent widths and the other which forced the width to be equal. For the latter type, the

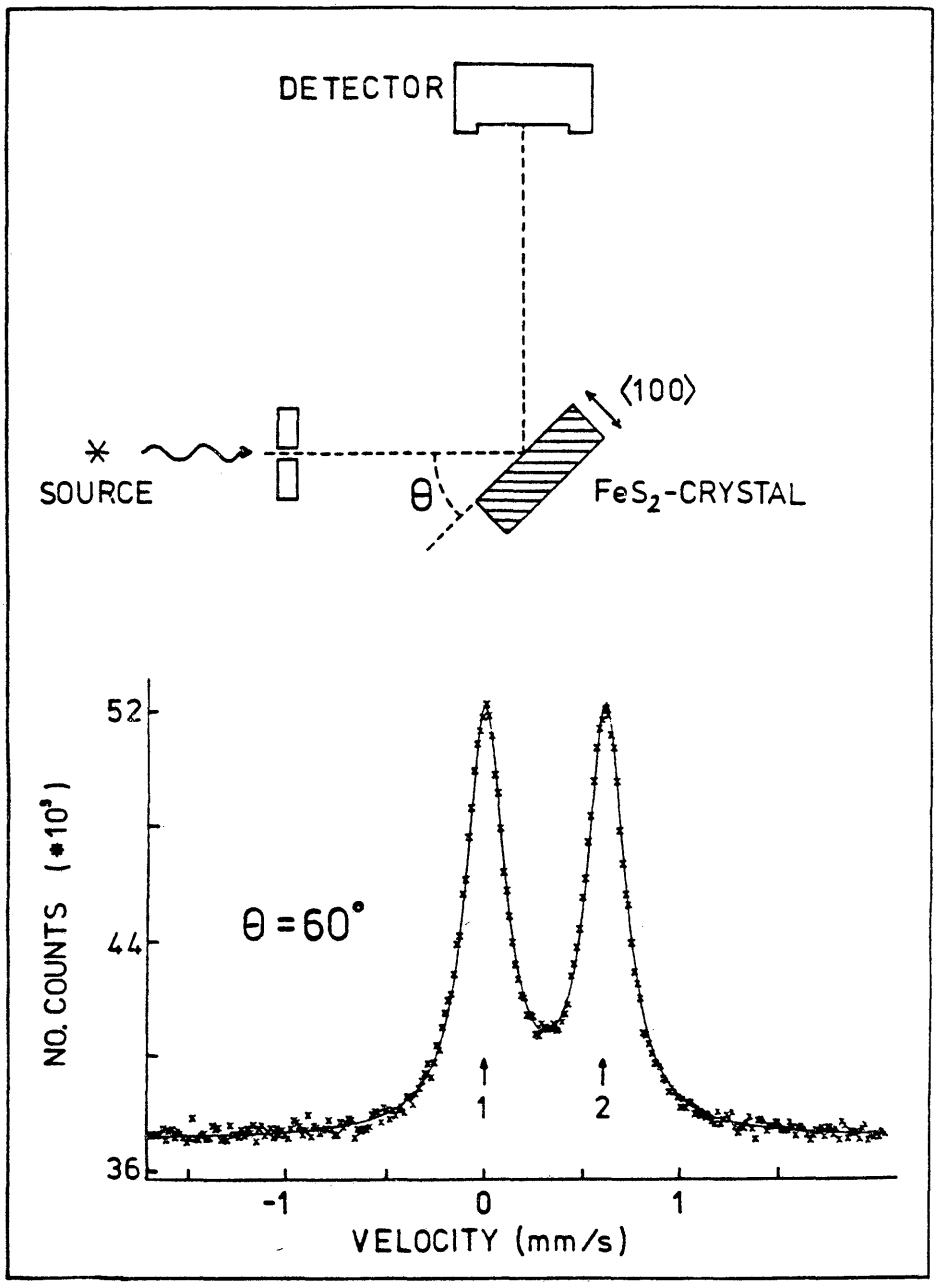

Fig. 2.1. Experimental Set-up and Mössbauer spectrum obtained with 6.3 keV internal conversion X-ray. The counter position was adjustable such that data could be obtained for θ up to 90°.

area ratio was thus reduced to an intensity ratio, resulting in smaller statistical uncertainties. In the following R is the ratio of the resonance area (width x intensity) of line 1 to line 2 (Fig. 2.1) from fit of two independent Lorentzians. R' is the ratio of the resonance intensity of line 1 to line 2 from fit of two lines with width forced to be equal.

2.2 Results and Discussion

Table 2.1 lists our results for various angles θ. We find all values of R and R' to be unity within one standard deviation with the exception of R for $\theta = 70^{o}$ which is within 1.7 standard deviations. The weighted average of the intensity ratio R' over all samples is 0.997 ± 0.004.

In addition to the results from the scattering of the 6.3 keV x-rays from the single crystal, Table 2.1 includes the result obtained from 14.4 keV γ-ray-transmission through a single crystal absorber of about 150μ thickness and the result from transmission spectra of powder samples of 32μ average particle size. Special care had to be taken in the preparation of the powder specimens due to the formation of $FeSO_4 \cdot H_2O$ (water soluble) in the grinding process. A small amount of this compound will cause the pyrite line 1 (Fig. 2.1) to appear more intense and could have been the cause of some of the discrepancies of earlier work (16,17,18). The narrow linewidth obtained in the scattering mode compared to the transmission mode for the 150μ specimen is indicative of the much smaller effective thickness sampled by the 6.3 keV x-rays.

Thus, experimentally, the area ratio of the two resonance lines obtained from the Mossbauer spectra of a single crystal of pyrite is unity within error, and independent of the orientation of the crystal axes to the incident γ-ray. This

TABLE 2.1. Results from computer analysis of Mössbauer data. θ is the angle defined in Figure 2.1. R is the ratio of resonance area (width x intensity) of line 1 to line 2 (Fig. 2.1) from fit of two independent Lorentzians. R' is the ratio of resonance intensity of line 1 to line 2 from fit of two lines with width constrained to be the same. Γ is the full width at half maximum in mm/s obtained from the latter type of fit. The uncertainties shown represent one standard deviation of statistical uncertainty from the computer fits.

θ	R	R'	Γ
SINGLE CRYSTAL - SCATTERING MODE			
45° ⟨110⟩	0.997 ± 0.014	0.994 ± 0.007	0.241 ± 0.001
60°	1.009 ± 0.016	1.001 ± 0.008	0.238 ± 0.001
70°	0.965 ± 0.021	0.995 ± 0.011	0.236 ± 0.001
80°	1.036 ± 0.037	0.998 ± 0.018	0.237 ± 0.002
90° ⟨100⟩	0.997 ± 0.038	0.988 ± 0.018	0.235 ± 0.002
	0.997 ± 0.009*	0.997 ± 0.004*	
SINGLE CRYSTAL - TRANSMISSION MODE			
90° ⟨100⟩	0.999 ± 0.010	1.000 ± 0.004	0.389 ± 0.002
POWDERS - TRANSMISSION MODE			
Random		1.0002 ± 0.0010**	0.253 ± 0.001

* Weighted average
** Average of 9 samples

agrees with the theoretical work of Liu and shows that the recoil-free fraction can be taken to be isotropic in pyrite. These conclusions are of current interest in the quantitative analysis of the pyrite content in coal and coal-derived products[21]. They permit one to disregard the orientation of pyrite crystals in a highly textured coal sample: for example, a determination of the amount of pyrite can be made solely from the observation of the intensity of one of the two lines in the Mossbauer spectrum.

3. EFFECT OF ABSORBER INHOMOGENEITY

When considering an absorber of uniform thickness in MES, it is well known that the total area of the observed resonance lines is not linear with increasing thickness due to saturation effects. This nonlinear behavior leads to a reduced resonance area for nonuniform absorbers of the same average thickness. This granularity effect is not simply due to electronic absorption as is often assumed.

Bowman et al.,[22] have treated the effect of powder absorbers in MES and developed equations describing the relative transmission and absorption linewidths. Abe and Schwartz[23] have determined the granularity effect on the absorption area for a six line absorber.

The following is a summary of their works and an extension to higher order corrections; in addition to their calculations, which assume granules of uniform size, a Gaussian size distribution will be considered.

3.1 Theory

In the thin source approximation, i.e. if the self-absorption of the source is negligible, the total area of the resonance lines in a multiline Mossbauer spectrum is given by[23]

$$A_{total} = f_S \int_{-\infty}^{\infty} \left[1 - \exp\left(- \sum_i q_i \sigma_i(E) \tau\right)\right] dE \qquad (3.1)$$

for a thin-foil absorber of uniform thickness t_A.

The parameters are defined as follows:

f_S = recoil-free fraction of the source

f_A = recoil-free fraction of the absorber

q_i = transition probability of the i-th line

$\sigma_i(E) = \dfrac{\Gamma^2/4}{(E-E_i)^2 + \Gamma^2/4}$ = nuclear resonance cross section

Γ = full width at half-height of emission and absorption lines centered at E_i

σ_o = absorption cross section at resonance

a_A = fractional abundance of the nuclei which can absorb resonantly

n_A = number of nuclei per cm^3

$\tau = f_A n_A a_A \sigma_o t_A$ = effective absorber thickness

In general q_i and f_A will depend on the angle of the incident γ-ray with respect to crystalline axes in the absorber. For pyrite, however, we have shown in section 2, that f_A (recoil-free fraction for a pyrite absorber) is angle-independent and that the two line intensities are equal i.e. $q_1 = q_2 = 1/2$.

We make the assumptions that the absorber and source linewidths are the same and equal to the natural linewidth[20] $\Gamma = 0.097$ mm/sec (^{57}Fe), i.e. the effects on line broadening due to varying local environments at the ^{57}Fe nuclei in pyrite, and any effects due to the overlap of the two resonance lines in pyrite are negligible.

Let us now consider an absorber consisting of a large number of granules distributed randomly throughout the absorber. We find that τ varies across this absorber and define the average effective thickness, i.e. the thickness the absorber would have if it were a uniform foil, as $T = \bar{n} \langle t \rangle$, where $\bar{n}$ is the average number of granules encountered by the γ-ray and $\langle t \rangle$ is the effective thickness of a single granule, averaged over its properties (size, shape). Assuming a Poisson distribution for the number of granules encountered[22] and small variances from uniform absorber thickness[22,23] ($\langle t \rangle << T$) one obtains by averaging eqn. (3.1) over all possible thicknesses encountered by the γ-rays, the area for one resonance line of pyrite

$$\langle A \rangle = f_S \int_{-\infty}^{\infty} (1 - e^{-q\sigma(E)T})\, dE - \frac{1}{2} f_S T \frac{\langle t^2 \rangle}{\langle t \rangle} X \int_{-\infty}^{\infty} (q^2\sigma^2(E) e^{-q\sigma(E)T}) dE + \frac{1}{6} f_S T \frac{\langle t^3 \rangle}{\langle t \rangle} X \int_{-\infty}^{\infty} (q^3\sigma^3(E) e^{-q\sigma(E)T}) dE - \ldots + \ldots \qquad (3.2)$$

where

$$T = f_A a_A \sigma_o n_A t_A = f_A a_A \sigma_o m \frac{N_o}{M} \equiv \epsilon t_A, \qquad (3.2a)$$

and

f_A = recoil-free fraction of pyrite

a_A = fractional abundance of ^{57}Fe = 0.0214 (natural)[24]

σ_o = absorption cross section = $(2.56 \pm 0.05) \times 10^{-18} cm^2$[25]

t_A = average sample thickness

N_o = Avogadro's number

M = atomic weight of Fe

m = mass of Fe per unit area of sample perpendicular to γ-ray beam

q = 0.5 for pyrite

From ByKov and Hien[26] an analytical expression for the first term in (3.2) can be given

$$f_S \int_{-\infty}^{\infty} (1 - e^{-q\sigma(E)T}) dE = f_S \frac{\pi}{2} \Gamma K(T) \qquad (3.3)$$

with $K(T) = qT\, e^{-qT/2} \left[I_o(qT/2) + I_1(qT/2) \right]$ where I_n are modified Bessel functions of n-th order.

The other integrals can also be evaluated in terms of the modified Bessel functions (Appendix A):

$$\langle A \rangle = f_S \frac{\pi}{2} \Gamma \left[K(T) - C_1(T, \langle t \rangle) + C_2(T, \langle t \rangle) - \ldots + \ldots \right] \qquad (3.4)$$

where

$$C_1(T,\langle t\rangle) = \frac{1}{4}\, T\, e^{-qT/2}\, q^2\, \frac{\langle t^2\rangle}{\langle t\rangle} \left[I_o(qT/2) - I_1(qT/2)\right] \quad (3.5)$$

$$C_2(T,\langle t\rangle) = \frac{1}{48}\, T\, e^{-qT/2}\, q^3\, \frac{\langle t^3\rangle}{\langle t\rangle} \left[3I_o(qT/2) - 4I_1(qT/2) + I_2(qT/2)\right] \quad (3.6)$$

The first term in (3.4) expresses the absorption area for a sample of uniform effective thickness T while the second and following terms account for the effect of granularity. For a given effective thickness T and transition probability q, the strength of each granularity term C_m is controlled by the shape of the particles and their size distribution in the absorber through the factor $\langle t^{m+1}\rangle/\langle t\rangle \equiv g_m$, hereafter referred to as the m-th granularity factor. Some of the g_m have been calculated for two different shapes, right circular cylinders whose axes are all parallel to the incident γ-rays and spheres, and for two types of size distribution functions, uniform and Gaussian. These are summarized in Table 3.1.

$p(t)dt$ is the probability that a gamma ray encounters a thickness between t and t + dt, such that $\int p(t)dt = 1$ and $\langle t^m\rangle = \int p(t)t^m dt$. In Table 3.1, t_o is the effective thickness averaged over all granules in the absorber, i.e. $t_o = \epsilon\langle d\rangle$ where $\langle d\rangle$ is the actually measured average size: length for cylinders and diameter for spheres; σ is the effective standard

shape	distribution p(t)	$\langle t \rangle$	g_1	g_2
right circular cylinders (axis $\parallel$ to γ-beam)	uniform thickness $\delta(t-t_o)$	t_o	t_o	t_o^2
	Gaussian thickness $\frac{1}{\sigma\sqrt{2\pi}} e^{-(t-t_o)^2/2\sigma^2}$	t_o	$t_o + \sigma^2/t_o$	$t_o^2 + 3\sigma^2$
spheres	uniform radius $2t/t_o^2$, $0 \le t \le t_o$	$\frac{2}{3} t_o$	$\frac{3}{4} t_o$	$\frac{3}{5} t_o^2$
	Gaussian radius $\int_{-\infty}^{\infty} C t\, e^{-(R-t_o/2)^2/2\sigma^2} dR$, $0 \le t \le 2R$ $C = \left[2\sigma\sqrt{2\pi}\left(\sigma^2 + t_o^2/4\right)\right]^{-1}$	$\frac{2}{3} t_o \left(\frac{3x+1}{x+1}\right)$ $x = 4\sigma^2/t_o^2$	$\frac{3}{4} t_o \left(\frac{3x^2+6x+1}{3x+1}\right)$ $x = 4\sigma^2/t_o^2$	$\frac{3}{5} t_o \left(\frac{15x^2+10x+1}{3x+1}\right)$ $x = 4\sigma^2/t_o^2$

TABLE 3.1. Granularity factors for right circular cylinders and spheres. The parameters are discussed in the text.

deviation $\sigma = \epsilon\sigma_{act}$, where σ_{act} is the measured standard deviation; and R is the effective radius. C follows from normalization. In obtaining the p(t) and g_m for spheres, the necessary integrations over R were performed from $-\infty$ to $+\infty$ to obtain closed forms. Since only $t, R \in [0,\infty]$ is physically possible, it is necessary to assume that the width of the distribution is less than t_o to ensure that only a small error results from the integration from $-\infty$ to 0.

In order to see the range of validity of the above approximation method we also evaluated the area of one resonance line directly, without small variance expansion, for right circular cylinders and spheres, including a Gaussian size-distribution in each, yielding (Appendix B)

$$\langle A\rangle = f_S \frac{\Gamma}{2} \int_0^{\pi} \left(1 - e^{-\bar{n}} \exp\left[\bar{n}\, e^{-q t_o \sin^2\theta} e^{q^2\frac{\sigma^2}{2}\sin^4\theta}\right]\right) \frac{1}{\sin^2\theta}\, d\theta \quad (3.7)$$

for cylinders, with $T = \bar{n}\, t_o$ and

$$\langle A\rangle = f_s \frac{\Gamma}{2} \int_{-\infty}^{\infty} \left(1 - e^{-\bar{n}} \exp\left\{\bar{n} \frac{1}{2p^2(\sigma^2+R_o^2)}\left[1 - e^{-2pR_o+2p^2\sigma^2}\right.\right.\right.$$

$$\left.\left.\left.(1 + 2pR_o - 4p^2\sigma^2)\right]\right\}\right) dE \quad (3.8)$$

for spheres, where $p = q\,\sigma(E)$ and $R_o = t_o/2$.

The modified Bessel functions and eqn. (3.7) can be evaluated numerically by computer using Gauss-Legendre Quadrature[27].

$$\int_0^{\alpha} f(x)dx = \sum_I \alpha\, W(I) f(\alpha\, R(I)) \qquad (3.9)$$

where R(I), W(I) are Legendre roots and weights[28] respectively and I = 48 for our calculations.

Fig. 3.1 is the theoretical plot of area versus effective thickness only, as given by eqn. (3.3). For large T the area becomes less sensitive to variations in T due to saturation. The top curve may reflect this more clearly as it shows the slope of the lower curve normalized to the slope at T = 0.

Fig. 3.2 shows the theoretical normalized results obtained from eqns. (3.4) and (3.7) for granules of right cylindrical shape. Curves (1) through (4) are calculated with the small variance approximation (3.4): (1) for the δ-function distribution evaluated to 1st order correction, (2) for the δ-function distribution evaluate to 2nd order correction; (3) and (4) for the Gaussian size distribution, calculated to 1st and 2nd order correction, respectively. Curve (5) is the result of the numerical evaluation of (3.7). Two sets of curves are plotted for T = 1.0 and T = 4.0. In the numerical evaluation for all these curves q was taken to be q = 0.5 as reference to pyrite and $\sigma = 0.5\ t_o$ (see section 3.2). The latter assumption ensures that the integration from $-\infty$ to $+\infty$ for the distribution causes small errors.

Several conclusions can be made from Fig. 3.2. The best approximation to the direct evaluation of the area ((5)) is given

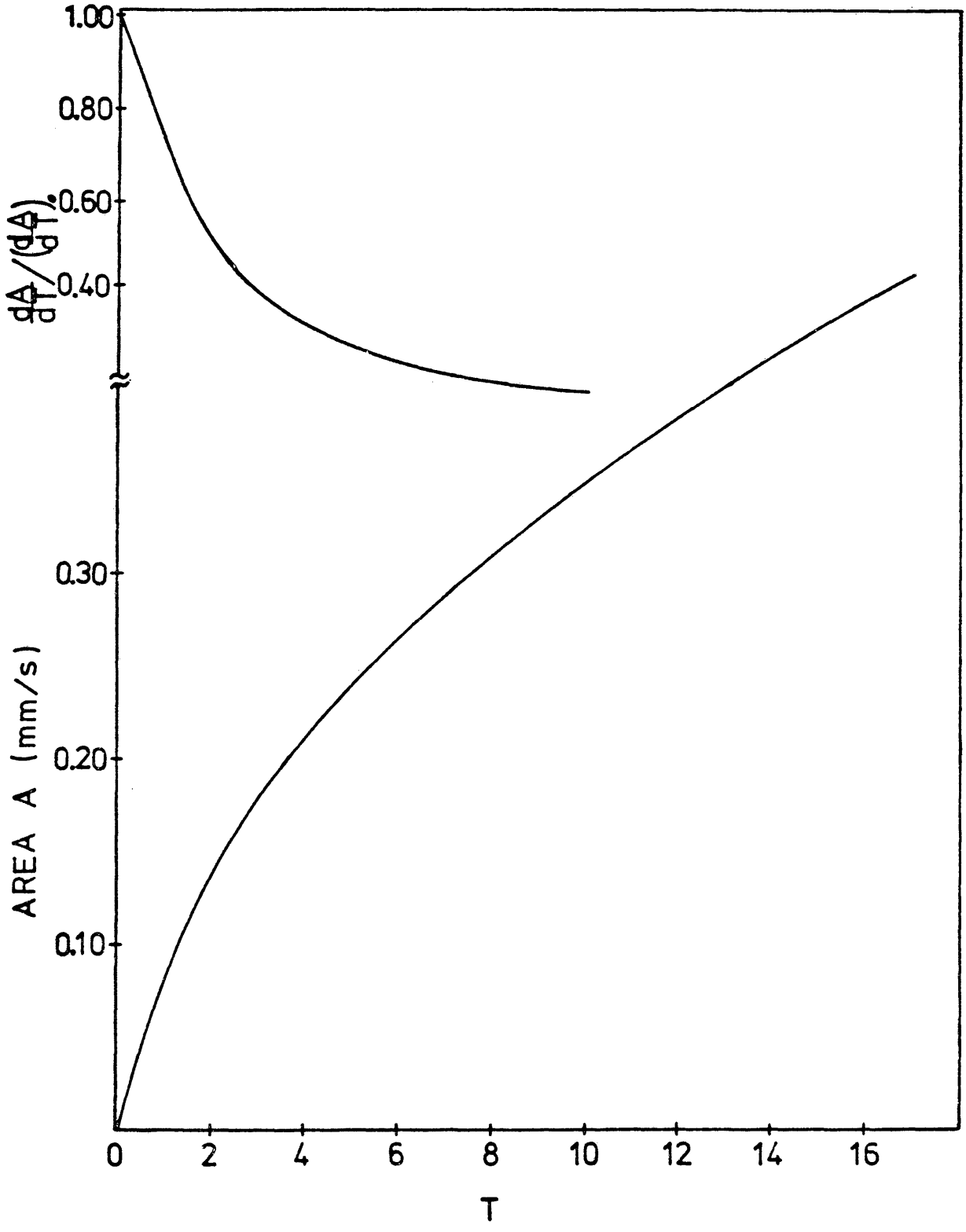

Fig. 3.1. Area vs. effective thickness T without granularity corrections.

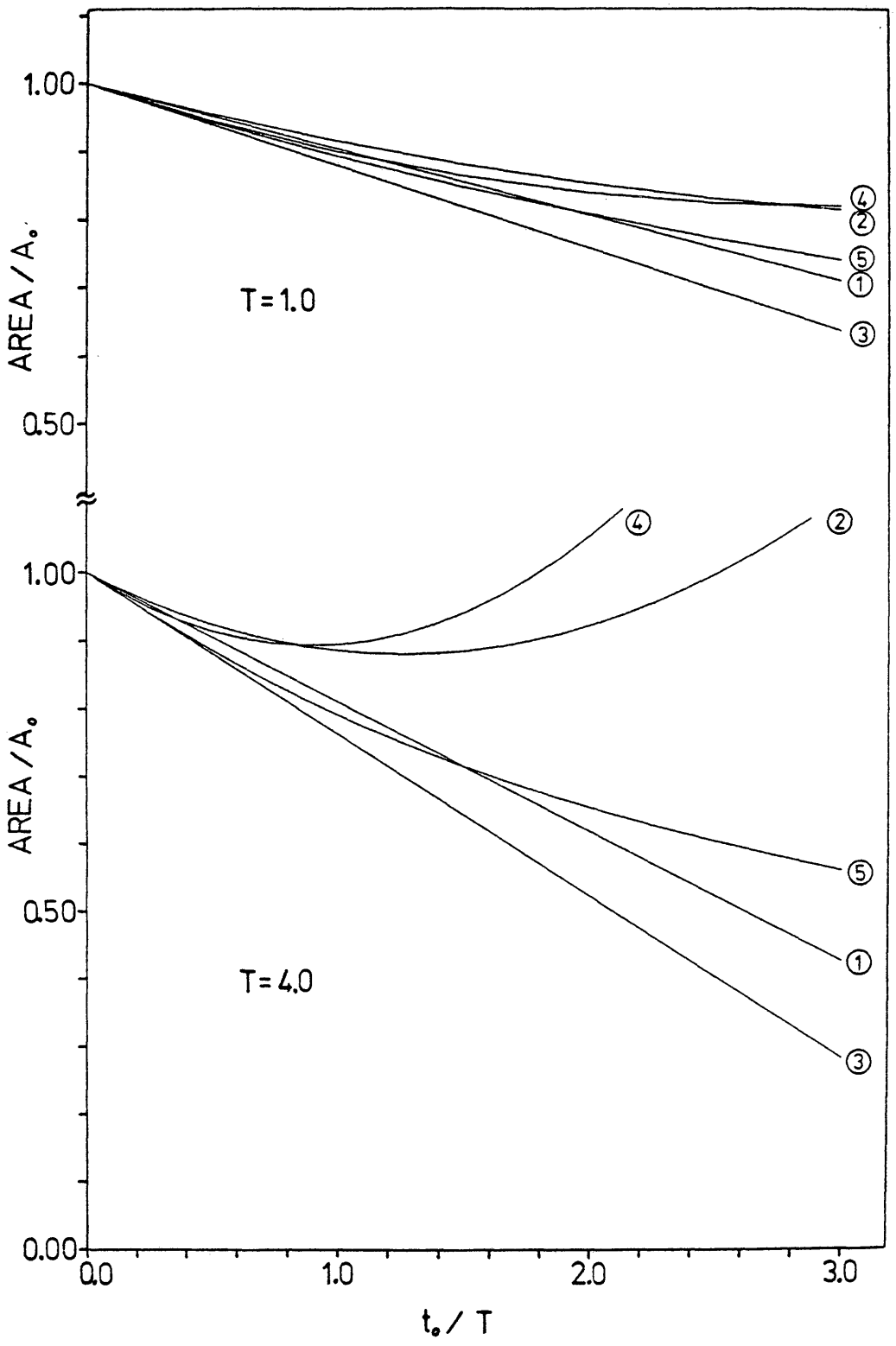

Fig. 3.2. Theor. results from eqns. (3.4),(3.7) for granules of right cylindrical shape. The parameters and curves are explained in the text.

by the evaluations that include only the linear corrections ((1),(3)), particularly in the region where $t_o/T \leq 1.0$. The inclusion of the 2nd order correction term ((2),(4)) causes a strong deviation from the direct evaluation ((5)); if a 3rd order correction were included one would probably obtain a better approximation due to its subtractive property; corrections should therefore be carried out to odd orders. Including a Gaussian particle size distribution in the area evaluation results in an increased slope, comparing curve (3) to (1). This can also be seen in the values g_1/t_o given in Table 3.2 which lists the theoretical factors g_m/t_o^m for the two shapes and distributions mentioned before. The values of g_m/t_o^m using the Gaussian distribution in (3.4) are strongly dependent on the choice of σ.

The most important result from Fig. 3.2 is the strong decrease of A with increasing granule thickness t_o (as seen by curve (5)); this may result in errors in the experimental area evaluation of 40% (if $t_o/T = t_o/4 = 3$).

Comparison of the two sets of curves, for T = 4.0 and T = 1.0, shows that the variation in A/A_o at $t_o/T = 1.0$ is less for the smaller T, i.e. the linear approximation (3) deviates less from the direct evaluation (5). For T = 1.0, the error in the experimental area evaluation is only 20% at $t_o/T = 3$, compared to the 40% for T = 4.0.

shape	distribution	g_1/t_o	g_2/t_o^2
cylinders	$\delta(t-t_o)$	1.00	1.00
	Gaussian	1.25	1.75
spheres	$2t/t_o^2$	0.75	0.60
	Gaussian	1.88	3.90

TABLE 3.2. Theoretical values for g_m/t_o^m.
In the evaluation using the Gaussian size distribution, the standard deviation was taken to be $\sigma = 0.5\, t_o$.

We may conclude, that the area determined experimentally from a granular absorber contains less error if the effective thickness of the absorber and its granules are small.

3.2 Experimental Procedure

To test the above theoretical effects of absorber inhomogeneity on the Mossbauer resonance area we prepared a series of pure pyrite absorbers of different but known granule sizes and distributions and obtained their Mossbauer spectra.

3.2.1 Equipment. The spectra were accumulated using a constant acceleration spectrometer consisting of a Multichannel Analyzer, a conventional feedback controlled driving unit and amplifier pulse height analyzer. The radiation source was about 25 mCi of ^{57}Co in a Pd matrix. The source Mossbauer fraction is $f = 0.660 \pm 0.003$[29] at 295K. The 14.4 keV gamma rays were detected with a Kr-CO_2 proportional counter. The velocity calibration was done by using a 25μ thick Fe-foil as an absorber and moving the source relative to the absorber. The line positions were then compared with known energies[24].

To ensure good statistics, off resonance counts of $5(10)^5$ to $1.8(10)^6$ per channel were accumulated. All measurements were made at room temperature.

3.2.2 Absorber Preparation. All absorbers used were powder specimens. The pyrite, in the form of naturally occuring crystals, was ground in a tungsten carbide shatterbox grinder and mechanically shaken through a set of standard sieves of mesh sizes 100, 150, 200, 275 and 400. The material which was minus 400 mesh was then separated into various sizes by a H_2O

Sub-Sieve Sizer (Cyclosizer). The mean size and size distribution of the particles in each sample was obtained by light-microscope. A polaroid photo was taken of the particles as shown in Fig. 3.3 for the particles of size 200-270 mesh. A transparency, produced from a photo of a 100 x 0.01 = 1mm graticule,taken with the same magnification, was then used to determine the size of a single granule by measuring its largest and smallest diameter and averaging. 100 granules were measured this way and their final sizes averaged to yield <d> and σ_{act} as listed in Table 3.3

Three amounts of each size were weighted out: 21.8 mg, 50.0 mg and 100.0 mg. In each case the pyrite was mixed with 0.5 g powdered confectioners sugar and mixed thoroughly for 2 min. with a Wig-L-Bug dental mixer. The powders were then compressed into 2.54 cm diameter pellets at 6 kpsi in a specimen mount press and sealed between two strips of masking tape.

We thus had absorbers of each size of 4.30 mg FeS_2/cm^2, 9.87 mg FeS_2/cm^2 and 19.74 mg FeS_2/cm^2; an additional sample of 33.91 mg FeS_2/cm^2 of each size was obtained by stacking the first three. These orders of weights of pyrite are commonly found in Mossbauer absorbers prepared from coals. Another reason for choosing these small amounts lies in their small average thickness t_A, so that saturation effects (Fig.

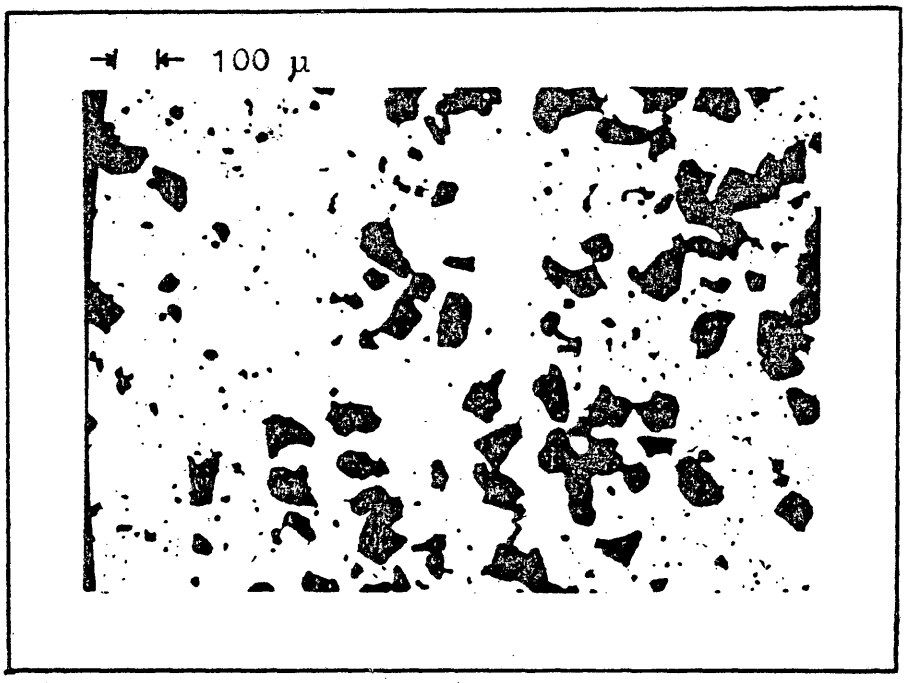

Fig. 3.3. Photo of particles of size 200 to 270 mesh.

from mesh	$\langle d \rangle \pm \sigma_{sd}$ (μ)
100 - 150	125 ± 30
150 - 200	90 ± 20
200 - 270	64 ± 15
270 - 400	45 ± 12
minus 400	48 ± 10
	39 ± 10
	29 ± 11
	19 ± 8

TABLE 3.3. Average pyrite particle sizes as used in the experiments.

3.1) are kept small. With the density of pyrite $\rho = 5.013$ g/cm^3 the average thickness are $t_A = 8.58\mu$, 19.68μ, 39.37μ and 67.63μ, respectively.

The samples were checked for uniformity by examining the transmission count rate of 14.4 keV γ-radiation through an area of 0.64 cm diameter at several points of a given sample; the variations stayed within 2%.

The collimated beam of γ-rays was kept at 0.64 cm diameter for all Mossbauer spectra.

A word of caution is in place here with respect to quantitative analysis of pure pyrite. Quite often iron sulfate, $FeSO_4.H_2O$, occurs with pyrite, on its surface or its surrounding environment; the presence of a resulting second quadrupole pair in the Mossbauer spectrum must be included in the transition probabilities and in the weight concentrations. Since $FeSO_4$ is water soluble it can easily be removed. Care must also be taken in the choice of laboratory grinders, an Fe-based grinder will produce considerable contamination because of the extreme hardness of pyrite.

3.2.3 Background Correction. Since we are only interested in observing the 14.4 keV gamma rays it is necessary to account for other radiation having similar energy, i.e. background[30, 31]. A small percentage of the background is due to natural radiation; most of it is produced by radiation from the source.

The primary radiation from the source consists of 14.4, 122 and 136 keV gamma rays and 6-7 keV x-rays produced by K capture and internal conversion in the iron. There are also higher energy gammas due to radiochemical impurities in the ^{57}Co and x-rays from other materials in source, absorber and surroundings due to photoelectric effect with the high energy radiation.

One method of accounting for this background is to insert a 0.005 in. (0.127mm) thick brass foil between absorber and detector[30]. This filter will allow less than 0.02% of the 14.4 keV gamma rays through while removing only 4% of the high energy radiation[31].

The background factor, when using the brass filter method, is given by

$$B = (1 - 1.04\ F_1/F_2)^{-1} \qquad (3.10)$$

where F_1, F_2 are the number of counts with and without brass filter respectively, when observing the 14.4 keV gammas in transmission.

An alternative method to account for the background is to calculate the area under the 14.4 keV peak in the pulse height spectrum. The background factor is then

$$B = \frac{A_B + A_{14.4}}{A_{14.4}} \qquad (3.11)$$

A_B and $A_{14.4}$ are shown in Fig. 3.4.

We evaluated both methods experimentally by observing the count rate in a fixed time interval of the 14.4 keV gamma through the 19.74 mg FeS_2/cm^2 sample of smallest particle size (19μ). The number of counts with and without the brass filter were inserted in equation (3.10) to obtain B and from the spectra B was evaluated by (3.11). This was done by averaging over different counting times.

In addition the sensitivity of B to the window setting of the multichannel analyzer (Fig. 3.4) of the 14.4 keV peak was examined.

The results are summarized in Table 3.4. The variation of B from the two methods is less than 2%. The setting we used to obtain our pyrite spectra lies close to setting 2 where B was typically about 1.05 for all samples.

Fig. 3.5 shows a typical pulse height spectrum obtained with and without brass filter. The brass filter method was used to determine the background in all pyrite samples. The background factor B must be included in equation (1.12) and the experimental area of the i-th line is now

$$A_i = B \frac{\pi}{2} \frac{\Gamma_i I_i}{N_\infty} \tag{3.12}$$

The last column in Table 3.4 shows the sensitivity of the total area A to the experimental window setting for the pyrite sample.

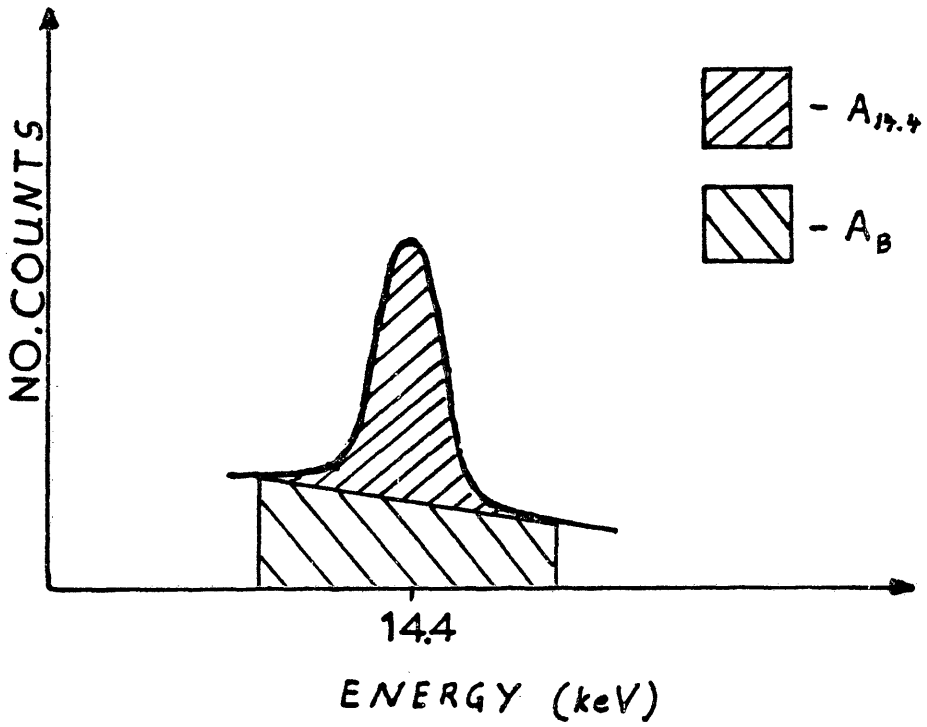

Fig. 3.4. Areas for evaluation of the background factor by the pulse height method. A_B is from background radiation.

window-setting	B*	B**	A (mm/s)
1	1.100	1.119	0.239
2	1.070	1.087	0.243
3	1.042	1.063	0.239
4	1.030	1.026	0.227

TABLE 3.4. Evaluation of the background factor B. The window narrows from setting 1 to 4. 2 is the usual setting for our measurements, at the beginning of the up-slopes. The 14.4 keV γ-rays were observed.

* - B from brass filter method.

** - B from area evaluation.

A is calculated from eqn. (3.12) for the 19.7 mg FeS_2/cm^2 sample(19 μ).

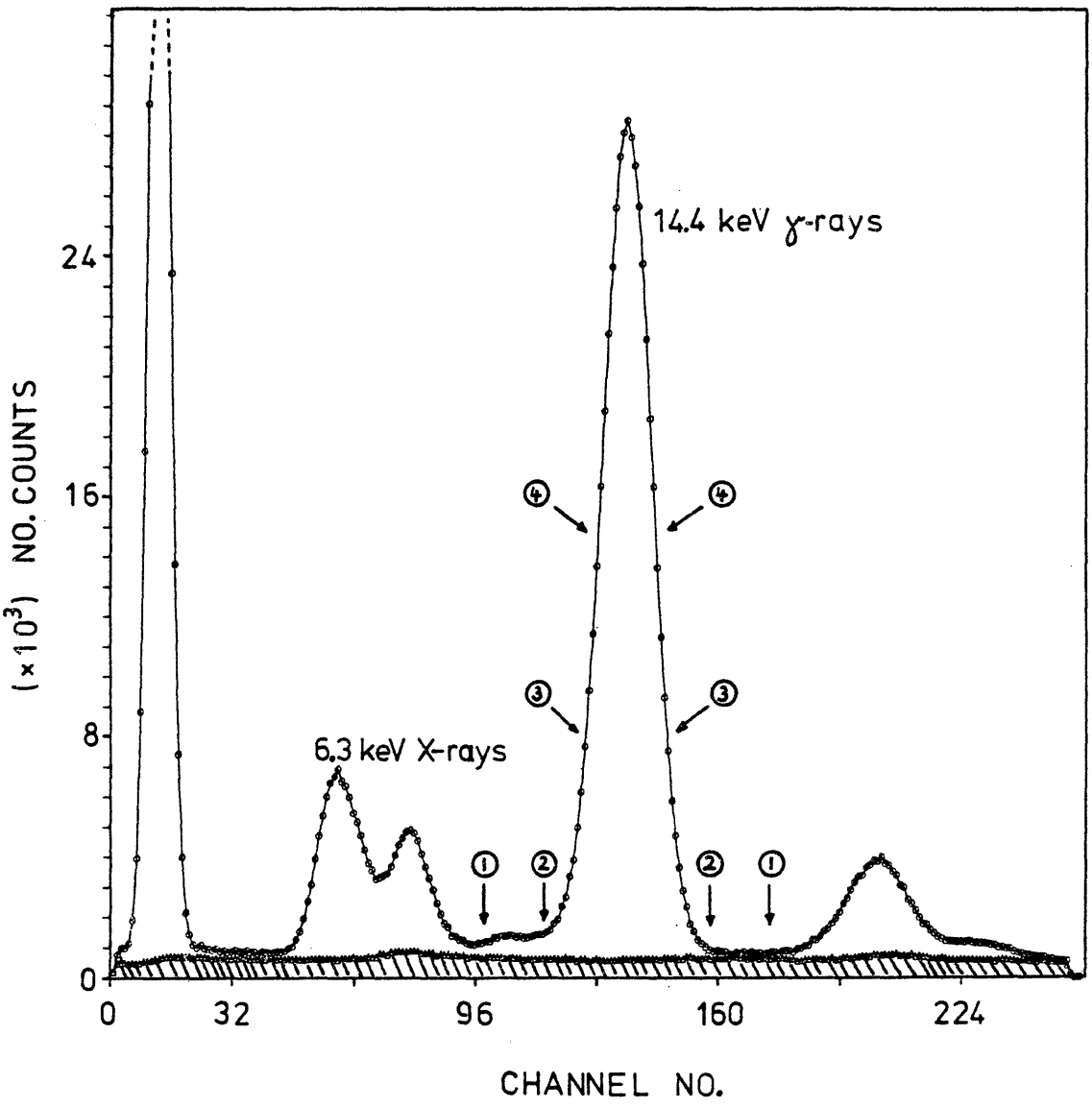

Fig. 3.5. Pulse height spectrum.

o- spectrum without brass filter.

▲- background observed with brass filter.

Arrows indicate window settings.

3.2.4 Data Reduction. The reduction was done by least-squares fitting of Lorentzians to the experimental data. Due to the slight overlap of the two resonance lines in the Mossbauer spectra of pyrite the linewidths were forced to be equal in the fits; this results in smaller statistical uncertainties. Since we have shown the line intensities to be equal for pyrite (Section 2), there is no physical reason for unequal line widths.

3.3 Experimental Results and Discussion

The effect of granularity on the area of the spectral lines for pyrite is most impressively demonstrated by Fig. 3.6. Shown are the spectra for the 19.7 mg FeS_2/cm^2 samples of 19μ and 125μ size. As expected from the theoretical results, Fig. 3.2, the area for the 19μ size sample is significantly larger than for the 125μ size sample.

This can also be concluded from Fig. 3.7, showing the experimental areas of one of the transition lines of pyrite as a function of sample weight and average particle size. The vertical arrows indicate the average thickness, t_A, for each sample weight as evaluated in section 3.2.2. The solid lines passing through each set at constant weight are least square polynomial fits of the form

$$A = A'_o + A'_1 \langle d \rangle + A'_2 \langle d \rangle^2 + \ldots \qquad (3.13)$$

The obtained fit parameters A'_o, A'_1, A'_2 can be compared with the theoretical calculations (3.4) to (3.6) to yield the recoil-free fraction of pyrite and some of the granularity parameters g_m. A'_o is independent of $\langle d \rangle$ and comparing (3.13) with (3.4) yields

$$A'_o = f_s \frac{\pi}{2} \Gamma K(T) \qquad (3.14)$$

we can thus solve for T, which can only be done numerically,

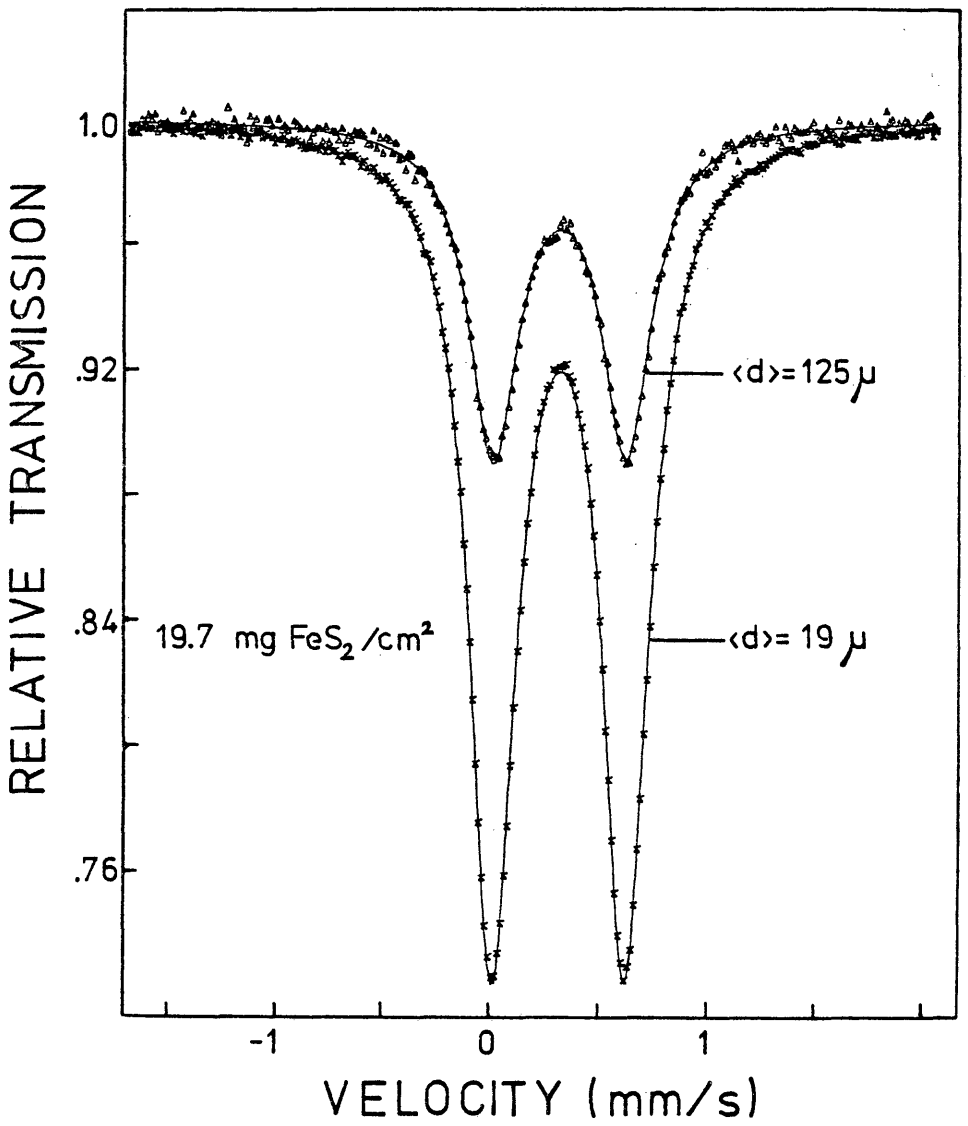

Fig. 3.6. Normalized spectrum of the 19.7 mg FeS_2/cm^2 absorbers of particle size 19μ and 125μ.

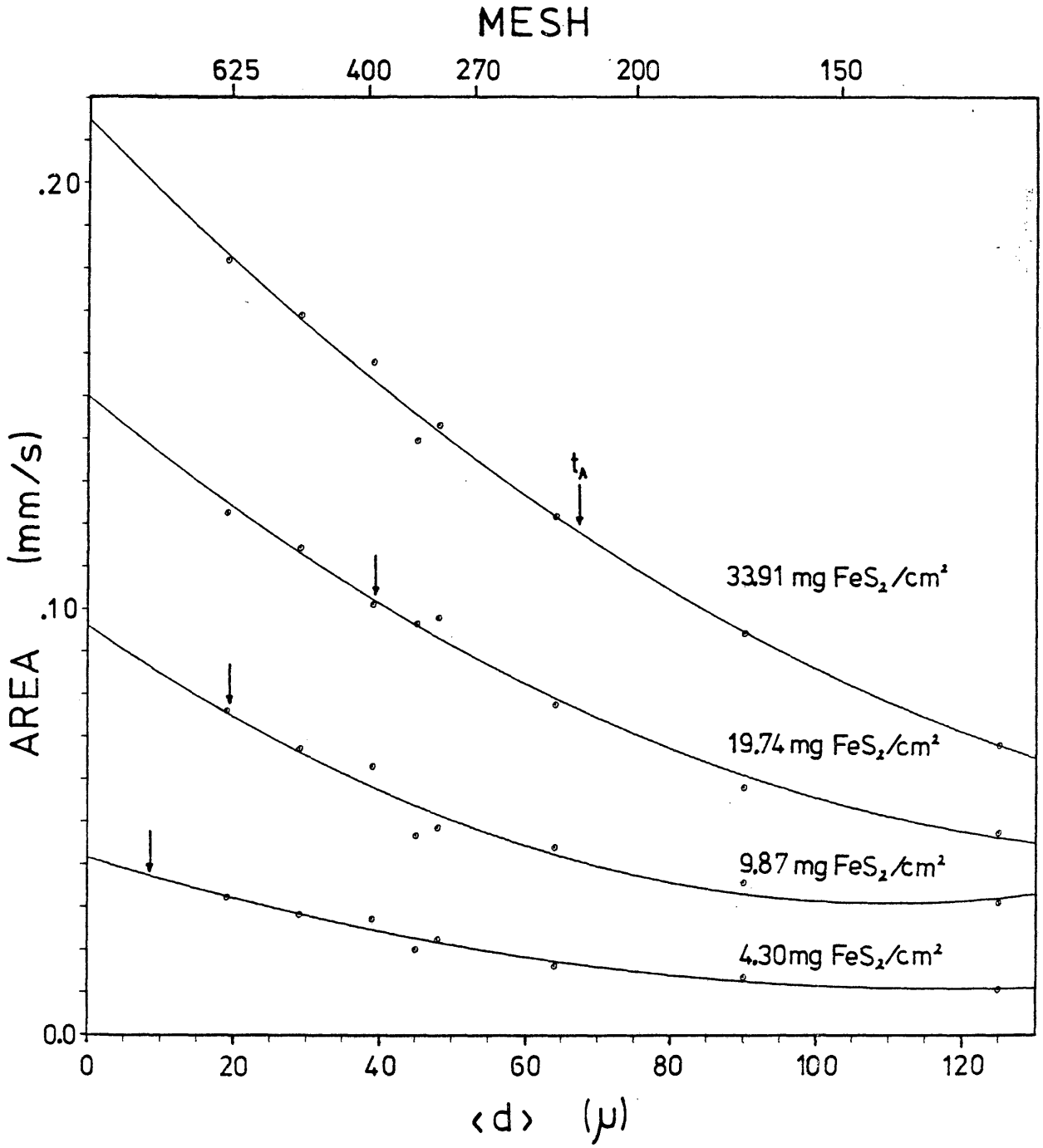

Fig. 3.7. Experimental area of right transition line of pyrite vs. particle size.
The solid lines are least square polynomial fits.

and in turn obtain f_A for pyrite from eqn. (3.2a). By analogous comparison one obtains g_1/t_o and g_2/t_o^2 from A_1' and A_2' respectively, where $t_o = \epsilon\langle d\rangle$, and $\langle d\rangle$ is from Table 3.3.

The values for f_A, g_1/t_o and g_2/t_o^2 found experimentally for each weight are given in Table 3.5. The average value for the recoil-free fraction of pyrite is $f_A = 0.86 \pm 0.06$.

From Fig. 3.2 in section 3.1 we concluded that the theoretical approximation given by the linear first order correction is better than that which includes the second order correction. With this in mind only the first four data points (approximately the linear portion), of each set at constant weight, i.e. for $\langle d\rangle$ = 19μ, 29μ, 39μ and 48μ, were fitted with eqn. (3.13) and from the resulting A_o' and A_1' the values f_A and g_1/t_o were calculated, as given in Table 3.6. The average value for the recoil-free fraction of pyrite thus obtained is $f_A = 0.80 \pm 0.08$.

Two other values have so far been found for the recoil-free fraction of pyrite; Montano [2] reports $f_A = 0.60 \pm 0.07$ based on the Debye model and 77K and 295K measurements and from reference (8), Fig. 10, a value $f_A = 0.48$ can be obtained. However, Montano has not considered the possible effect of granularity on the determination of the Debye temperature in his pyrite powder absorbers and in reference (8) the effects due to absorber inhomogeneity and background radiation have been neglected.

weight (mg FeS_2/cm^2)	f_A	g_1/t_o	g_2/t_o^2
4.30	0.78	1.17	0.39
9.87	0.92	1.44	0.47
19.74	0.85	1.90	0.56
33.91	0.88	3.12	0.97

TABLE 3.5. Experimental values for the recoilfree fraction f_A of pyrite and for the granularity factors.
The average value for f_A is 0.86 ± 0.06.

weight (mg FeS_2/cm^2)	f_A	g_1/t_o
4.30	0.71	0.83
9.87	0.89	1.12
19.74	0.77	1.33
33.91	0.83	2.34

TABLE 3.6. Experimental values for f_A and g_1/t_o from fitting the linear portion of each data-set only.
The average value for f_A is 0.80 ± 0.08.

The experimentally obtained granularity factors g_1/t_o, as shown in Table 3.5 and 3.6, agree relatively well with the theoretical values and are in better agreement with the Gaussian model calculations (Table 3.2). The experimental values for the 33.91 mg FeS_2/cm^2 sample are substantially larger than the theoretical values. This may be the result of stacking 3 absorbers and needs to be investigated further. There is also a systematic increase of g_1/t_o with sample weight and g_2/t_o^2 is experimentally smaller than theoretically predicted which may be due to a limitation in our models. These results require further study.

The dependence of f_A of pyrite on our model parameters has been considered. The two shapes assumed for the granules and the two size distribution cause variations in f_A as given in Table 3.7. The 19.7 mg FeS_2/cm^2 sample with the smallest average size granules ($\langle d \rangle = 19\mu$, $\sigma = 8\mu$) was considered, since the granularity effect should be minimum. The f_A-values were obtained numerically by comparing the experimental area to the theoretical area from eqn. (3.4), with correction to second order, for the two shapes and distribution and to the theoretical area from eqn. (3.7) for cylindrical granules with Gaussian size distribution. The variation in f_A is less than 7%. For the same sample, Table 3.8 reflects the dependence of f_A on the standard deviation σ_{act} when evaluated from

shape, method	distrib.	f_A
cylinders, small variance Eqn.(3.4)	$\delta(t-t_o)$	0.71
	Gaussian	0.72
spheres, small variance Eqn.(3.4)	$2t/t_o^2$	0.70
	Gaussian	0.74
cylinders, direct evaluation Eqn.(3.7)	Gaussian	0.75

TABLE 3.7. Dependence of f_A of pyrite on granule shape and distribution for the 19.74 mg FeS_2/cm^2 sample, $\langle d \rangle = 19\mu$, $\sigma_{act} = 8\mu$.

$\langle d \rangle$ (μ)	σ_{act} (μ)	f_A
19	5	0.74
	10	0.76
	15	0.80

TABLE 3.8. Sensitivity of f_A on variations of σ_{act} for 19.74 mg FeS_2/cm^2.

the comparison of the experimental area with the theoretical area from eqn. (3.7). The actual standard deviation for this sample is $\sigma_{act} = 8\mu$ (Table 3.3).

An error analysis performed for the recoil-free fraction f_A of pyrite due to errors in the Mossbauer parameters involved, e.g. the absorption cross section σ_o of ^{57}Fe, the errors in the weights, shows an error of 2.4%. Thus, the main source of the error obtained for our recoil-free fraction $f_A = 0.80 \pm 0.08$ comes from absorber preparation, from size analysis of the granules in a given sample and from inaccuracies in our model.

4. CONCLUSIONS

The foregoing sections result in two major conclusions: the angle independence of the Mossbauer effect in single crystal pyrite and the necessity of considering the effect of granularity in the quantitative analysis of pyrite.

Two approaches are thus possible to determine the amount of pyrite in a powder sample from the area of one of the two Mossbauer transition lines:

i) prepare an absorber of small average effective thickness and containing extremely small granules such that $t_o/T \ll 1$, and the effect of granularity becomes negligible, or

ii) prepare an absorber such that $t_o/T \leq 1$ and account for granularity in the calculation of the area using the first order correction developed here. Prior knowledge of average granule size and distribution is required. The theory will not be accurate for $t_o/T > 1$.

In either case one wishes to keep T small to minimize the effect due to saturation.

We found the recoil-free fraction of pyrite to be $f = 0.80 \pm 0.08$ when accounting for granularity and background radiation. This value is higher than two others found to date.

The purpose of this work was to clarify two of the problems one is confronted with in quantitative analysis of pyrite in coal. The pyrite used in our experiments was taken from naturally occuring crystals. In coal however, pyrite occurs in various sizes and forms, from framboidal clusters[10] to large chunks and may have different properties due to impurities. This might result in the recoil free fraction being different from the value given above. Also, FeS_2 has a metastable phase, marcasite, which has slightly different values for the isomer shift and quadrupole splitting and occurs in coal[10]. If the recoil free fraction, f, for marcasite is substantially different than the value for pyrite, an error in the evaluation of the amount of the pyritic iron in the coal will result if the marcasite is not accounted for.

In the theoretical calculations performed here the assumptions were made that source and absorber line widths were the same and equal to the natural line width and that the effect of overlap of the resonance lines is negligible. Careful investigation needs to be done to determine to what extent the resulting calculations vary, if these assumptions are not made.

Finally, we suggest that experiments be done with a series of coals which have been carefully characterized with regard to their pyrite particle size distribution and their pyrite content (by methods other than MES) in order to test the theoretical granularity corrections developed here.

REFERENCES

1. J.F. Lefelhocz, R.A. Friedel and T.P. Kohman, Geochim Cosmochim Acta, 31, 2261 (1976).

2. P.A. Montano, Fuel, 56, 397 (1977).

3. L.M. Levinson and I.S. Jacobs, Fuel, 56, 453 (1977).

4. G.V. Smith, J. Liu, M. Saporoschenko and R. Shiley, Fuel, 57, 41 (1978).

5. I.S. Jacobs, L.M. Levinson and H.R. Hart, Jr., J. Appl. Phys, 49, 1975 (1978).

6. P.E. Russell and P.A. Montano, J. Appl. Phys. 49, 1573 (1978).

7. A.H. Stillert, JJ. Renton, P.A. Montano and P.E. Russell, Fuel, 57, 447 (1978).

8. G.P. Huffman and F.E. Huggins, Fuel, 57, 592 (1978).

9. B. Keisch, G.A. Gibbon and S. Akhtar, Fuel Processing Tech., 1, 269 (1977/78).

10. P.A. Montano, Preprints of Am. Chem. Soc., Div. of Fuel Chem. 24, 218 (1979).

11. R.D. Cole. J. Liu, G.V. Smith, C.C. Hinckley and M. Saporoschenko, Fuel, 57, 514 (1978).

12. U. Gonser, Ed., Mossbauer Spectroscopy, Topics in Appl. Phys., Vol. 5, Springer (1975).

13. P. Gütlich, R. Link and A. Trautwein, Mossbauer Spectroscopy and Transition Metal Chem., Inorganic Chem. Concepts, Springer (1978).

14. G.K. Wertheim, Mossbauer Effect: Principles and Application, Academic Press (1964).

15. A. Serres, J. Phys. Radium, 14, 689 (1953).

16. S.L. Finklea and L. Cathey, Acta Cryst. A32, 529 (1976).

17. I.P. Suzdalev, I.A. Vinogradov and V.U. Imshennik, Soviet Phys. Solid State, 14, 1136 (1972).

18. V.K. Garg, Y.S. Liu and S.P. Puri, J. Appl. Phys. 45, 70 (1974).

19. Y.S. Liu, Phys. Rev. B20, 71 (1979); J. Physique, C2, 400 (1979).

20. N. Abe and L.H. Schwartz, Mat. Sci. Eng. 14, 239 (1974).

21. D.L. Williamson, T. Guettinger and D.W. Dickerhoof, Bull. APS 24, 299 (1979).

22. J.D. Bowman, E. Kankeleit, E.N. Kaufmann and B. Persson, Nucl. Instr. Meth. 50, 13 (1967).

23. N. Abe and L.H. Schwartz, in I.J. Gruverman (ed.), Mossbauer Effect Methodology, Vol. 8, Plenum (1973).

24. Mossbauer Effect Data Index, J.G. Stevens and V.E. Stevens (editors), IFI/Plenum (1978).

25. D.P. Johnson, Phys. Rev. B, 1, 3551 (1970).

26. G.A. ByKov and P.Z. Hien, Soviet Phys. JETP, 16, 646 (1963).

27. A. Ralston, A First Course in Numerical Analysis, McGraw Hill (1965).

28. C.H. Love, Abscissas and Weights for Gaussian Quadrature, Natl. Bureau of Standards, NBS Monograph 98 (1966).

29. R.H. Nussbaum, D.G. Howard, W.L. Nees and C.F. Steen, Phys. Rev. 173, 653 (1968).

30. D.P. Johnson and J.G. Dash, Phys. Rev. 172, 983 (1968).

31. R.M. Housley, N.E. Erickson and J.G. Dash, Nucl. Instr. Meth. 27, 29 (1964).

APPENDIX A

Evaluation of the 1st and 2nd order correction term in terms of modified Bessel functions.

From eqns. (3.2), (3.4) one finds

$$C_1(T,<t>)f_S\,\Gamma\frac{\pi}{2} = \frac{1}{2}\,f_s\,T\,\frac{<t^2>}{<t>}\int_{-\infty}^{\infty} q^2\sigma^2(E)\,e^{-q\sigma(E)T}\,dE \qquad (A1)$$

$$C_2(T,<t>)f_S\,\Gamma\frac{\pi}{2} = \frac{1}{6}\,f_S\,T\,\frac{<t^3>}{<t>}\int_{-\infty}^{\infty} q^3\sigma^3(E)\,e^{-q\sigma(E)T}\,dE \qquad (A2)$$

where

$$\sigma(E) = \frac{\Gamma^2/4}{(E-E_o)^2 + \Gamma^2/4}$$

Denoting the integrals in (A1) and (A2) by J_1 and J_2 respectively and using the substitution $p = 2(E - E_o)/\Gamma$ one obtains

$$J_1 = \frac{\Gamma}{2}\int_{-\infty}^{\infty} q^2\left(\frac{1}{1+p^2}\right)^2 e^{-qT/1+p^2}\,dp \qquad (A3)$$

$$J_2 = \frac{\Gamma}{2}\int_{-\infty}^{\infty} q^3\left(\frac{1}{1+p^2}\right)^3 e^{-qT/1+p^2}\,dp \qquad (A4)$$

To perform the integrals one uses the substitution $p = \tan\theta$ $p\varepsilon\left[-\infty,\infty\right]$ results in $\theta\varepsilon\left[-\frac{\pi}{2}, \frac{\pi}{2}\right]$, $dp = 1/\cos^2\theta\,d\theta$ and $(1+p^2)^{-1} = \cos^2\theta$ to yield

$$J_1 = \frac{\Gamma}{2}\,q^2\int_{-\pi/2}^{\pi/2}\cos^2\theta\,e^{-qT\cos^2\theta}\,d\theta = 2q^2\,\frac{\Gamma}{2}\int_{o}^{\pi/2}\cos^2\theta\,e^{-qT\cos^2\theta}\,d\theta \qquad (A5)$$

$$J_2 = \frac{\Gamma}{2} q^3 \int_{-\pi/2}^{\pi/2} \cos^4\theta \; e^{-qT\cos^2\theta} d\theta = 2q^3 \frac{\Gamma}{2} \int_o^{\pi/2} \cos^4\theta \; e^{-qT\cos^2\theta} d\theta \tag{A6}$$

With

$$\cos^2\theta = \frac{1}{2}(1 + \cos 2\theta) \text{ and } \cos^4\theta = \frac{1}{8}(3 + 4\cos 2\theta + \cos 4\theta)$$

and by setting $2\theta = \phi$, such that $\theta \epsilon \left[0, \frac{\pi}{2}\right]$ yields $\phi \epsilon \left[0, \pi\right]$ and $d\theta = \frac{1}{2} d\phi$ (A5) and (A6) become

$$J_1 = \frac{1}{2} q^2 e^{-qT/2} \frac{\Gamma}{2} \int_o^{\pi} e^{-(qT/2)\cos\phi} (1 + \cos\phi) \, d\phi \tag{A7}$$

$$J_2 = \frac{1}{8} q^3 e^{-qT/2} \frac{\Gamma}{2} \int_o^{\pi} e^{-(qT/2)\cos\phi} (3 + 4\cos\phi + \cos 2\phi) \, d\phi \tag{A8}$$

The modified Bessel functions are defined as

$$I_n(x) = \frac{1}{\pi} \int_o^{\pi} e^{x\cos\phi} \cos(n\phi) \, d\phi \tag{A9}$$

and have the properties

$$\begin{aligned} I_o(-x) &= I_o(x) \\ I_1(-x) &= -I_1(x) \\ I_2(-x) &= I_2(x) \end{aligned} \tag{A10}$$

Thus we obtain

$$J_1 = \frac{\pi}{2} q^2 e^{-qT/2} \frac{\Gamma}{2} \left[I_o(qT/2) - I_1(qT/2)\right] \tag{A11}$$

$$J_2 = \frac{\pi}{8} q^3 e^{-qT/2} \frac{\Gamma}{2} \left[3I_o(qT/2) - 4I_1(qT/2) + I_2(qT/2)\right] \tag{A12}$$

Using these expressions one obtains from (A1) and (A2)

$$C_1(T,\langle t\rangle) = \frac{1}{4} Te^{-qT/2} q^2 \frac{\langle t^2\rangle}{\langle t\rangle} \left[I_o(qT/2) - I_1(qT/2)\right]$$

$$C_2(T,\langle t\rangle) = \frac{1}{48} T e^{-qT/2} q^3 \frac{\langle t^3\rangle}{\langle t\rangle} \left[3I_o(qT/2) - 4I_1(qT/2) + I_2(qT/2)\right]$$

as given in (3.5) and (3.6)

APPENDIX B

Development of equations (3.7) and (3.8).

From Bowman et al.[22] we find for the resonance area of one line

$$\langle A\rangle = \sum_{n=o}^{\infty} Pn \left\langle f_s \int_{-\infty}^{\infty} (1 - e^{-q\sigma(E)\tau}) dE \right\rangle_n \qquad (B1)$$

when considering an absorber consisting of a large number of randomly distributed granules. $\tau = \sum_{i=1}^{n} t_i$ is the total thickness of the absorbing material where t_i is the thickness encountered in the i^{th} granule. Since we assume a large number of granules (about 10^4 to 10^6 in each of our samples), whose locations may be considered independent, we may use the Poisson distribution $P_n = \bar{n}^n e^{-\bar{n}}/n!$, where $\bar{n}$ is the average number encountered by a gamma ray, P_n is the probability that n granules are encountered, $\langle\ \rangle_n$ denotes the conditional expectation over those paths of the γ-ray which intersect n granules.

With these considerations the order of integration and summation may be reversed to give

$$\langle A\rangle = f_s \int_{-\infty}^{\infty} \left(\sum_{n=o}^{\infty} \frac{e^{-\bar{n}}\bar{n}^n}{n!} \langle 1 - e^{-q\sigma(E)\tau} \rangle_n \right) dE$$

$$= f_s \int_{-\infty}^{\infty} \left(\sum_{n=o}^{\infty} \frac{e^{-\bar{n}}\bar{n}^n}{n!} - \sum_{n=o}^{\infty} \frac{e^{-\bar{n}}\bar{n}^n}{n!} \langle e^{-q\sigma(E)\tau} \rangle_n \right) dE \qquad (B2)$$

Using the properties of Poisson distribution and the fact that the t_i are independent (B2) becomes

$$\langle A\rangle = f_s \int_{-\infty}^{\infty} \left[1 - \sum_{n=o}^{\infty} \frac{e^{-\bar{n}}\bar{n}^n}{n!} \left(\langle e^{-q\sigma(E)t}\rangle_g\right)^n\right] dE \qquad \text{(B3)}$$

where $\langle \quad \rangle_g$ denotes the average over the properties of a single granule. The sum can be written in closed forms as

$$\langle A\rangle = f_s \int_{-\infty}^{\infty} \left(1 - \exp\left[-\bar{n}\left(1 - \langle e^{-q\sigma(E)t}\rangle_g\right)\right]\right) dE$$

$$= f_s \int_{-\infty}^{\infty} \left(1 - e^{-\bar{n}}\, e^{\bar{n}\langle e^{-q\sigma(E)t}\rangle_g}\right) dE \qquad \text{(B4)}$$

Let $p(t)dt$ be the probability that a granule displays a thickness between t and dt, when encountered by a gamma-ray. Then

$$\langle e^{-q\sigma(E)t}\rangle_g = \int p(t)\, e^{-q\sigma(E)t}\, dt \qquad \text{(B5)}$$

at this point the distributions given in Table 3.1 may be inserted. The following calculations are performed for right cylindrical granules, whose axes are parallel to the γ-ray direction and whose sizes are represented by a Gaussian distribution. Then

$$p(t) = \frac{1}{\sigma\sqrt{2\pi}} \exp\left[-\frac{(t-t_o)^2}{2\sigma^2}\right] \qquad \text{(B6)}$$

$$\text{and } \langle e^{-q\sigma(E)t}\rangle_g = \exp\left(-\sigma(E)q\,t_o + \sigma^2(E)q^2\,\frac{\sigma^2}{2}\right) \tag{B7}$$

In the evaluation of (B7) the integration in (B5) has been taken from $-\infty$ to ∞ to obtain a closed form solution. Physically, however $t\varepsilon[0,\infty]$ is only possible and $(t_o - \sigma) \geq 0$. We must therefore assume, that $\sigma < t_o$ to ensure that the error resulting from the integration from $-\infty$ to 0 is negligible. Then

$$\langle A\rangle = f_s \int_{-\infty}^{\infty} \left(1 - e^{-\bar{n}} \exp\left[\bar{n}\, e^{-\sigma(E)qt_o + \sigma^2(E)q^2\sigma^2/2}\right]\right) dE \tag{B8}$$

Let $p = 2(E-E_o)/\Gamma$, as in Appendix A, then $\sigma(E) = \frac{1}{1+p^2}$ and $E = \frac{\Gamma}{2}\,dp$ and (B8) becomes

$$\langle A\rangle = f_s \frac{\Gamma}{2} \int_{-\infty}^{\infty} \left(1 - e^{-\bar{n}} \exp\left[\bar{n}\, e^{-qt_o/1+p^2}\; e^{(1/1+p^2)^2 q^2\sigma^2/2}\right]\right) dp \tag{B9}$$

Now substitute $p = \operatorname{cotan}\theta$, then $p\varepsilon[-\infty,\infty]$ yield $\theta\varepsilon[\pi,0]$, $dp = -\frac{1}{\sin^2\theta}\,d\theta$ and $\frac{1}{1+p^2} = \sin^2\theta$ and we obtain

$$\langle A\rangle = f_s \frac{\Gamma}{2} \int_{\pi}^{o} \left(1 - e^{-\bar{n}} \exp\left[\bar{n}\, e^{-qt_o\sin^2\theta}\; e^{q^2(\sigma^2/2)\sin^4\theta}\right]\right) \left(-\frac{1}{\sin^2\theta}\right) d\theta$$

$$= f_s \frac{\Gamma}{2} \int_{o}^{\pi} \left(1 - e^{-\bar{n}} \exp\left[\bar{n}\, e^{-qt_o\sin^2\theta}\; e^{q^2(\sigma^2/2)\sin^4\theta}\right]\right) \frac{1}{\sin^2\theta}\; d\theta \tag{B10}$$

where $\bar{n} \langle t \rangle = T$, as in eqn. (3.7).

Eqn. (3.8) is obtained by inserting $p(t,R) = Ct\, e^{-(R-t_o/2)^2/2\sigma^2}$, given in Table 3.1, into

$$\langle e^{-q\sigma(E)t} \rangle_g = \int_{-\infty}^{\infty} \int_{o}^{2R} p(t,R) e^{-q\sigma(E)t}\, dt\, dR \qquad (B11)$$

to allow closed form solutions R is taken from $-\infty$ to ∞, assuming again $\sigma < t_o$. The rest follows analogous to above calculations.

APPENDIX C

Table of experimental data as used in Fig. 3.7 which shows A_2 vs. <d>.

Sizes 125μ to 45μ were taken directly from the sieves, sizes 48μ to 19μ were separated in a cyclosizer as described in section 3.2.2.

The spectra were fitted with least square Lorentzians. For spectras from samples of weights 33.91, 19.74, 9.87 mg FeS_2/cm^2 the linewidths were forced to be equal, thus R' is the ratio of resonance intensity of line 1 to line 2 (Fig.2.1). R for samples of weight 4.30 mg FeS_2/cm^2 is the ratio of the resonance area of line 1 to line 2 from fit of two independent Lorentzians.

<d> is the average size of the granules in a sample.

δ is the isomer shift.

Δ is the quadrupole splitting.

Γ is the linewidth found from fits when forced equal.

Γ_1 is the linewidth of line 1, Γ_2 is the linewidth of line 2 from independent fit.

A_1 is the area of line 1.

A_2 is the area of line 2.

B is the background factor found with the brass filter method.

Sample weight: 33.91 mg FeS_2/cm^2

<d> (μ)	δ (mm/s)	Δ (mm/s)	Γ (mm/s)	A_1 (mm/s)	A_2 (mm/s)	R'	B
19	0.3075±0.0011	0.6139±0.0020	0.2956±0.0013	0.1810±0.0010	0.1818±0.0010	0.9957±0.0039	1.1527
29	0.3079±0.0011	0.6146±0.0020	0.2886±0.0014	0.1683±0.0010	0.1689±0.0010	0.9963±0.0046	1.1362
39	0.3077±0.0011	0.6149±0.0020	0.2870±0.0014	0.1572±0.0009	0.1579±0.0009	0.9958±0.0044	1.1265
48	0.3080±0.0011	0.6146±0.0020	0.2830±0.0012	0.1433±0.0007	0.1431±0.0007	1.0012±0.0038	1.1165
45	0.3072±0.0011	0.6162±0.0020	0.2867±0.0014	0.1420±0.0008	0.1394±0.0008	1.0180±0.0045	1.1256
64	0.3075±0.0011	0.6169±0.0020	0.2864±0.0013	0.1236±0.0006	0.1218±0.0006	1.0149±0.0040	1.1190
90	0.3077±0.0011	0.6165±0.0020	0.2818±0.0013	0.0955±0.0005	0.0943±0.0005	1.0131±0.0044	1.0956
125	0.3077±0.0011	0.6167±0.0021	0.2854±0.0016	0.0683±0.0005	0.0680±0.0005	1.0053±0.0060	1.0837

Sample weight: 19.74 mg FeS_2/cm^2

19	0.3091±0.0011	0.6136±0.0019	0.2621±0.0010	0.1226±0.0005	0.1226±0.0005	1.0005±0.0025	1.0555
29	0.3091±0.0011	0.6157±0.0019	0.2612±0.0010	0.1146±0.0005	0.1143±0.0005	1.0029±0.0024	1.0529
39	0.3093±0.0011	0.6157±0.0020	0.2585±0.0010	0.1009±0.0005	0.1010±0.0005	0.9989±0.0032	1.0483
48	0.3091±0.0011	0.6157±0.0020	0.2614±0.0011	0.0978±0.0005	0.0979±0.0005	0.9986±0.0035	1.0497
45	0.3088±0.0011	0.6185±0.0020	0.2679±0.0010	0.0980±0.0004	0.0965±0.0004	1.0165±0.0027	1.0520
64	0.3088±0.0011	0.6180±0.0020	0.2690±0.0013	0.0786±0.0004	0.0775±0.0004	1.0147±0.0044	1.0486
90	0.3089±0.0012	0.6179±0.0021	0.2679±0.0016	0.0588±0.0004	0.0580±0.0004	1.0145±0.0064	1.0430
125	0.3080±0.0013	0.6165±0.0024	0.2788±0.0022	0.0480±0.0005	0.0474±0.0005	1.0121±0.0091	1.0427

Sample weight: 9.87 mg FeS_2/cm^2

<d> (μ)	δ (mm/s)	Δ (mm/s)	Γ(mm/s)	A_1 (mm/s)	A_2 (mm/s)	R'	B
19	0.3089±0.0011	0.6122±0.0019	0.2411±0.0010	0.0764±0.0003	0.0760±0.0003	1.0058±0.0031	1.0317
29	0.3088±0.0011	0.6126±0.0020	0.2415±0.0010	0.0669±0.0003	0.0671±0.0003	0.9981±0.0036	1.0292
39	0.3081±0.0011	0.6118±0.0020	0.2434±0.0011	0.0628±0.0004	0.0629±0.0004	0.9989±0.0043	1.0291
48	0.3086±0.0011	0.6122±0.0020	0.2451±0.0010	0.0486±0.0002	0.0485±0.0002	1.0008±0.0034	1.0281
45	0.3080±0.0011	0.6138±0.0020	0.2509±0.0012	0.0474±0.0003	0.0467±0.0003	1.0156±0.0046	1.0280
64	0.3083±0.0011	0.6146±0.0020	0.2566±0.0012	0.0445±0.0002	0.0440±0.0002	1.0110±0.0041	1.0283
90	0.3075±0.0013	0.6134±0.0023	0.2699±0.0020	0.0358±0.0003	0.0357±0.0003	1.0011±0.0084	1.0239
125	0.3078±0.0012	0.6127±0.0022	0.2612±0.0019	0.0318±0.0003	0.0311±0.0003	1.0226±0.0080	1.0265

Sample weight: 4.30 mg FeS_2/cm^2

<d> (μ)	δ (mm/s)	Δ (mm/s)	Γ_1 (mm/s)	Γ_2 (mm/s)	A_1 (mm/s)	A_2 (mm/s)	R	B
19	0.3057±0.0011	0.6142±0.0014	0.2318±0.0021	0.2339±0.0021	0.0319±0.0003	0.0322±0.0003	0.9904±0.0148	1.0233
29	0.3047±0.0013	0.6143±0.0020	0.2320±0.0035	0.2476±0.0037	0.0264±0.0005	0.0282±0.0005	0.9363±0.0237	1.0228
39	0.3055±0.0013	0.6145±0.0020	0.2357±0.0036	0.2381±0.0036	0.0271±0.0005	0.0272±0.0005	0.9985±0.0255	1.0223
48	0.3063±0.0013	0.6124±0.0018	0.2470±0.0031	0.2452±0.0031	0.0225±0.0003	0.0224±0.0003	1.0049±0.0209	1.0220
45	0.3090±0.0016	0.6168±0.0029	0.2516±0.0029	0.2458±0.0028	0.0207±0.0003	0.0201±0.0003	1.0311±0.0194	1.0231
64	0.3089±0.0017	0.6186±0.0032	0.2578±0.0039	0.2519±0.0039	0.0168±0.0003	0.0163±0.0003	1.0326±0.0259	1.0227
90	0.3103±0.0018	0.6162±0.0033	0.2648±0.0046	0.2633±0.0046	0.0139±0.0003	0.0136±0.0003	1.0200±0.0295	1.0230
125	0.3105±0.0020	0.6159±0.0038	0.2760±0.0064	0.2709±0.0063	0.0109±0.0003	0.0108±0.0003	1.0151±0.0390	1.0224

Coefficients in eqn. (3.13) from least squares polynomial fits.

(a) are the coefficients obtained by fitting all data points.

(b) are the coefficients obtained by fitting only the first four data points (19u - 48u), approximately the linear portion of the curves.

A'_o, A'_1, A'_2 are explained in the text.

weight (mg/cm^2)	(a)			(b)	
	A'_o	A'_1	A'_2	A'_o	A'_1
33.91	0.2146	-1.7460×10^{-3}	4.5716×10^{-6}	0.2070	-1.3068×10^{-3}
19.74	0.1498	-1.4003×10^{-3}	4.5746×10^{-6}	0.1394	-9.0232×10^{-4}
9.87	0.0960	-1.1851×10^{-3}	5.3969×10^{-6}	0.0936	-8.8782×10^{-4}
4.30	0.0415	-5.1877×10^{-4}	2.1965×10^{-6}	0.0381	-3.1370×10^{-4}